Remote Control of Filchner-Ronne Ice Shelf Melt Rates by the Antarctic Slope Current

Christopher Y. S. Bull, Adrian Jenkins, Nicolas Jourdain, Irena Vaňková, Paul R. Holland, Pierre Mathiot, Ute Hausmann, Jean-Baptiste Sallée

JGR Oceans

RESEARCH ARTICLE
10.1029/2020JC016550

Remote Control of Filchner-Ronne Ice Shelf Melt Rates by the Antarctic Slope Current

Christopher Y. S. Bull[1,2], Adrian Jenkins[1,2], Nicolas C. Jourdain[3], Irena Vaňková[1], Paul R. Holland[1], Pierre Mathiot[3,4], Ute Hausmann[5], and Jean-Baptiste Sallée[5]

[1]British Antarctic Survey, Cambridge, UK, [2]Department of Geography and Environmental Sciences, Northumbria University, Newcastle Upon Tyne, UK, [3]Universite Grenoble Alpes/CNRS/IRD/G-INP, IGE, Grenoble, France, [4]Met Office, Exeter, UK, [5]Sorbonne-Université, CNRS/IRD/MNHN (LOCEAN UMR 7159), Paris, France

Key Points:

- Filchner-Ronne Ice Shelf (FRIS) radar observations of basal melt rates are used to evaluate a regional Weddell Sea Nucleus for European Modeling of Ocean model configuration
- FRIS melt/freeze rate is quasi-linearly related to salinity changes in Antarctic Slope Current (ASC; 32 year time-mean)
- ASC temperature variations are quadratically related to FRIS freezing but limited change to FRIS melting

Supporting Information:

- Supporting Information S1
- Movie S1
- Movie S2

Correspondence to:
C. Y. S. Bull,
christopher.bull@northumbria.ac.uk

Citation:
Bull, C. Y. S., Jenkins, A., Jourdain, N. C., Vaňková, I., Holland, P. R., Mathiot, P., et al. (2021). Remote control of Filchner-Ronne ice shelf melt rates by the Antarctic slope current. *Journal of Geophysical Research: Oceans*, *126*, e2020JC016550. https://doi.org/10.1029/2020JC016550

Received 26 JUN 2020
Accepted 5 JAN 2021

Abstract Recent work on the Filchner-Ronne Ice Shelf (FRIS) system has shown that a redirection of the coastal current in the southeastern Weddell Sea could lead to a regime change in which an intrusion of warm Modified Circumpolar Deep Water results in large increases in the basal melt rate. Work to date has mostly focused on how increases in the Modified Circumpolar Deep Water crossing the continental shelf break leads directly to heat driven changes in melting in the ice-shelf cavity. In this study, we introduce a Weddell Sea regional ocean model configuration with static ice shelves. We evaluate a reference simulation against radar observations of melting, and find good agreement between the simulated and observed mean melt rates. We analyze 28 sensitivity experiments that simulate the influence of changes in remote water properties of the Antarctic Slope Current on basal melting in the FRIS. We find that remote changes in salinity quasi-linearly modulate the mean FRIS net melt rate. Changes in remote temperature quadratically vary the FRIS net melt rate. In both salinity and temperature perturbations, the response is rapid and transient, with a recovery time-scale of 5–15 years dependent on the size/type of perturbation. We show that the two types of perturbations lead to different changes on the continental shelf, and that ultimately different factors modulate the melt rates in the FRIS cavity. We discuss how these results, are relevant for ocean hindcast simulations, sea level, and melt rate projections of the FRIS.

Plain Language Summary Ocean water temperature or the speed of ocean currents can directly influence the melt rate of the floating ice shelves at the edge of the Antarctic Ice Sheet. Ice sheet modelers use simple relationships between ocean temperature and ice-shelf melt rates to create projections of sea level rise, whereby changes in salinity are not directly considered. Here, using a model of the ocean and ice shelf for the Weddell Sea region, we re-visit these relationships in a simulated environment with realistic settings. We find that changes in far field salinity and temperature in the Antarctic Slope Current can cause changes in the Filchner-Ronne Ice Shelf melt rate; this is because both far field temperature and salinity variations have the capacity to change the strength of the ocean circulation in the ice shelf cavity. Our results suggest that future numerical simulations of this region may need to consider changes in both far field temperature and salinity.

1. Introduction

The Filchner-Ronne Ice Shelf (FRIS), located at the southern boundary of the Weddell Sea, is the largest volume of floating ice in the world (Nicholls et al., 2009). Its tributary ice streams have a combined discharge of over 254 Gigatons yr^{-1}, draining ~15% of the Antarctic ice sheet by mass (Rignot et al., 2013). Several factors influence the environment that determines an ice shelf's basal melt rate, including: ice draft and bathymetry (Wei et al., 2019), sea ice growth (Markus et al., 1998), katabatic and large-scale wind patterns (Holland et al., 2019), and proximity to the shelf break of: Warm Deep Water (WDW), High Salinity Shelf Water (HSSW), Modified WDW (MWDW), and the Antarctic Circumpolar Current. With these factors in mind, the ice shelf's environment can be dynamically categorized in terms of a "cold" or "warm" regime (modes 1 and 2 in Jacobs et al., 1992, respectively), where FRIS is historically a cold regime ice shelf. For additional background, see Nicholls et al. (2009) for FRIS melt rates and relevant water masses on the surrounding continental shelf, Vernet et al. (2019) for a summary of present knowledge on the regional circulation and Dinniman et al. (2016) for a modern modeling perspective on ice shelf regimes. Future projections by Hellmer et al. (2012, 2017) suggest that the intrusion of warm water could lead to a tipping point where FRIS

could transition to a warm regime. First-order questions remain, however, as to the dynamical balances that drive the FRIS ocean cavity circulation and subsequent melt rates.

The relevant large-scale processes determining the FRIS overturning circulation and melt rates are summarized as follows. The Antarctic Slope Current (ASC) advects WDW (Circumpolar Deep Water's cooler and fresher derivative) along the continental slope (Thompson et al., 2018). The ASC is mostly wind driven, with the maximum speeds (6–9 cm/s) found during winter (May-June) when the wind forcing is strongest and the slope current is barotropic (Núñez-Riboni & Fahrbach, 2009). Where the WDW crosses the continental shelf edge, it mixes toward the surface, freshening and cooling along the way to form MWDW. In the late Austral summer (January-May), this modified water mass crosses the shelf break (Ryan et al., 2017). We will now summarize the local processes related to the FRIS cavity ocean circulation.

Seasonally strong sea ice formation across the continental shelf of the southwestern Weddell Sea creates HSSW. Brine rejection from sea ice production leads to the increased salinity in HSSW and the surface water mass is set to the surface freezing point. The HSSW formation also destratifies the water column near the ice shelf front, preventing intrusions of relatively warm MWDW. HSSW is sufficiently dense to flow into the FRIS cavity as a gravity current and, due to the pressure dependence of the freezing point as the HSSW sinks, it is able to melt ice, creating lighter Ice Shelf Water (ISW) that is buoyant enough to rise along the ice shelf base. Again, due to the pressure dependence of the freezing point, as the ISW rises it will at times refreeze to the ice shelf base. In addition to, the above processes driving the strength of the overturning circulation in the cavity, the tides drive stronger background flow speeds, resulting in a mean melt rate that is dominated by the tidal signal (Hausmann et al., 2020; Makinson et al., 2011; Mueller et al., 2018; Vaňková et al., 2020).

Improving our understanding of these ocean processes and the dynamical balances driving FRIS melt rates is crucial if we wish to provide accurate representations of the ice shelf for future ocean/ice-sheet coupled simulations. Several observational and modeling studies have focused on the processes controlling the FRIS ocean circulation and melt rates. Hellmer et al. (2012) used an ocean model forced by output from HadCM3-B run under the A1B emissions scenario to show that a redirection of the coastal current into the Filchner Trough could lead to warmer waters (+2°C absolute) entering the ice-shelf cavity, driving dramatic increases in basal melting (from 0.2 m/y to ~4 m/y). They suggest that the changes are driven by an increase in ocean surface stress in the southeastern Weddell Sea due to reduced sea ice cover. The follow up paper (Hellmer et al., 2017), suggested that, once the FRIS transitioned to a "warm regime" state, the changes would be irreversible. Darelius et al. (2016) and Ryan et al. (2017) examined observations including moorings, seal data and conductivity, temperature, and depth profiles to show that seasonal pulses of warm water arrive at the Filchner ice-shelf front; however, they did not find any evidence that these pulses enter the cavity. Daae et al. (2018) applied idealized modeling from Daae et al. (2017) to analyze warm water inflows in the observations, suggesting that strong winds drive a recirculation of the slope current carrying additional warm water into the Filchner Trough. Recently, Naughten et al. (2019) showed that offshore polynyas in the Weddell Sea can increase the transport of WDW across the shelf through density changes above the shelf break. Hazel and Stewart (2020) suggest that decreasing the meridional winds by 50% can switch FRIS from a cold to warm state. In the broader context, several modeling studies in the Amundsen Sea have reported changes in far-field forcing as a contributing factor to Circumpolar Deep Water crossing the shelf (Donat-Magnin et al., 2017; Nakayama et al., 2018; Spence et al., 2017; Webb et al., 2019). In summary, the studies above have focused on processes controlling the amount of heat fluxed across the shelf and their subsequent direct impact on melt rates in the cavity.

In an idealized modeling configuration without tides, Holland et al. (2008) formed much of the modern basis for our understanding of ocean climate sensitivity in terms of ice shelf melt rates. Specifically, Holland et al. (2008) studied the relationship between changes in ocean temperatures and melting in an ice-shelf cavity. They found basal melt to be quadratically related to far-field ocean temperature, while salinity changes were unimportant. The quadratic sensitivity to ocean temperature is routinely applied in modeling studies (DeConto & Pollard, 2016; Favier et al., 2019; Jourdain et al., 2020; Pollard & Deconto, 2012) and has been observed for the Dotson Ice Shelf (Jenkins et al., 2018). In some cases, the melt rate parameterization and sensitivity is more complex; for example, the Potsdam Ice-shelf Cavity mOdel (PICO) (Reese, Albrecht et al., 2018) has a quadratic or linear sensitivity in cold and warm water ice shelves, respectively. For a

review, see Asay-Davis et al., 2017). As far as, we are aware, ice-shelf melt sensitivity to far field temperatures and salinities has not been re-visited in a more realistic modeling setting (e.g., complex bathymetry, ice-shelf geometry, tides, and sea ice) nor in the context of a "cold water" ice shelf.

Over different time periods and different observationally based products, Figure 1 shows there are large differences in time-mean far field temperature and salinity in the ASC upstream of FRIS. Whilst observational data is limited in terms of trends for this region, a NEMO global simulation (described in Section 2.1) has a warming and freshening trend over the re-analysis period (Figure 1g). The influence of differences in temperatures and salinities such as those shown in Figure 1 on FRIS ocean circulation and melt rates was unknown, and will be explored in the present study.

The goal of this study is to examine the possible influence of changes in water mass properties in the ASC offshore of the continental shelf in relation to FRIS melt rates. Here, we use a 1/4° regional NEMO ocean configuration, which includes tides and static ice shelves (see Section 2.1); the configuration is based on the 1/12° version developed by Hausmann et al. (2020). We begin with an assessment of the historical time-mean ocean state and a comparison of simulated FRIS melt rates to melt rates derived from autonomous phase-sensitive radio-echo sounder (ApRES) observations (Vaňková et al., 2020). We then examine a hierarchy of simulations in which the upstream ASC is perturbed with temperature and salinity anomalies, leading to changes in the ocean cavity circulation and FRIS melt rates. The paper is presented as follows. Model description and experiment design are in Sections 2.1 and 2.2, respectively. Model evaluation is in Section 3.1. Results demonstrating the role of salinity and temperature in modulating the FRIS melt rate are shown in Section 3.2. Discussion and a summary are given in Sections 4 and 5, respectively.

2. Model and Experimental Design

2.1. WED025 NEMO Model and Its Configuration

The ocean general circulation model used in this study is version v3.6 of the Nucleus for European Modeling of Ocean model (NEMO; Madec, 2016), which includes the Louvain-la-Neuve sea ice model LIM-3.6 (Rousset et al., 2015). NEMO solves the incompressible, Boussinesq, hydrostatic primitive equations with a split-explicit free-surface formulation. NEMO here uses a z*-coordinate (varying cell thickness) C-grid with partial cells at the bottom-most and top-most ocean layers in order to provide more realistic representation of bathymetry (Barnier et al., 2006) and the ice-shelf draft, respectively. Our model settings include: 75 vertical levels, a 55-term polynomial approximation of the reference thermodynamic equation of seawater (TEOS-10; IOC 2010), nonlinear bottom friction, a no-slip condition at the lateral boundaries (at both land and ice shelf interfaces), energy- and enstrophy-conserving momentum advection scheme and a prognostic Turbulent Kinetic Energy (TKE) scheme for vertical mixing. Laterally, we have spatially varying eddy coefficients (according to local mesh size) with a Laplacian operator for iso-neutral diffusion of tracers and a biharmonic operator for lateral diffusion of momentum. The configuration used here is based on, and is similar to, the 1/12° Weddell Sea configuration developed by Hausmann et al. (2020); major differences include: coarser resolution, fewer tidal constituents and use of a new surface forcing (details below). In Hausmann et al. (2020), the 1/12° Weddell Sea configuration was evaluated in comparison to observations of the Weddell Sea system. With the exception of a strongly stratified summer seasonal thermocline and associated low bias in summer sea ice coverage, it was shown that, the overall circulation and water mass features in the deep, shelf, and cavity oceans are well represented in the reference simulation. The coarse resolution configuration employed here enables the use of many sensitivity experiments that would be impractical if a higher resolution configuration were used.

Our model setup utilizes the ice-shelf module that was developed by Mathiot et al. (2017). From a dynamical point of view, ice shelves affect the horizontal pressure gradient through the hydrostatic pressure exerted by ice on the ocean column and create friction at the top of the water column. As for bottom cells, the top cell thickness is adjusted to follow the actual ice draft, with an approach similar to the partial cells used by Barnier et al. (2006). Calculation of the ice shelf melt rate follows the standard three-equation parameterization as described in Asay-Davis et al. (2016), with heat exchange and salt exchange coefficients of $\Gamma_T = 1.4 \times 10^{-2}$ and $\Gamma_s = 4.0 \times 10^{-4}$, respectively. Additionally, the top drag coefficient is $C_d = 2.5 \times 10^{-3}$. The conservative temperature, absolute salinity, and velocity are averaged over the top mixed layer, defined

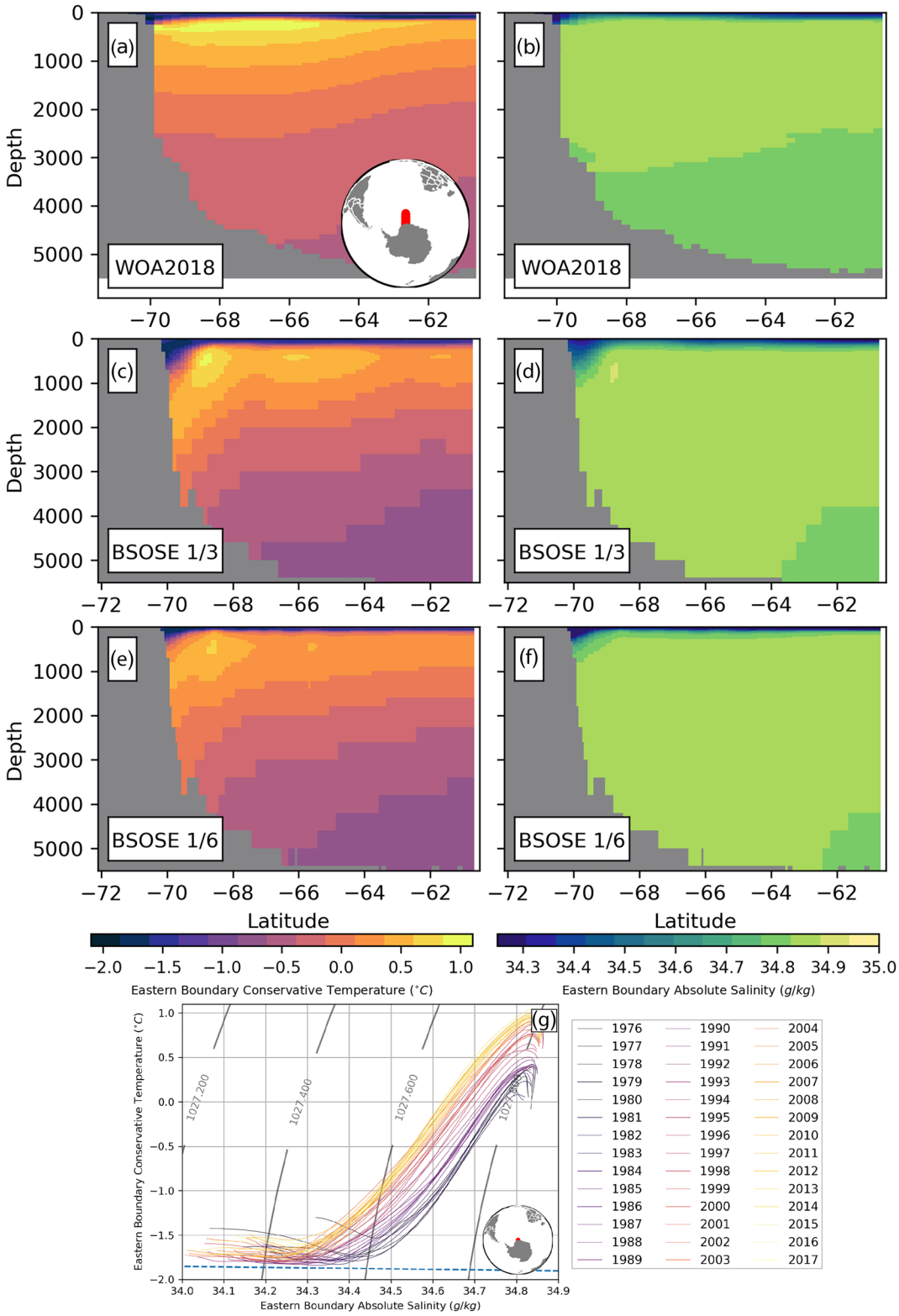

Figure 1. Comparison of Weddell Sea temperature and salinity across section pictured in inset in (a), for: (a-b) World Ocean Atlas 2018, (c-d) Biogeochemical Southern Ocean State Estimate (B-SOSE) 1/3° between January 1, 2008– January 31, 2012, (e-f) B-SOSE 1/6° January 1, 2013– December 31, 2017. (g) Temperature and Salinity trend during 1976–2017 at 69.7°S, −2.2°W (indicated in inset g) from a global NEMO simulation that is similar to Storkey et al. (2018)'s GO7 but forced by JRA. Section shown in a-f is the same as the eastern boundary of our regional simulations (Section 2 and red line Figure 2a). The G07-JRA time-mean eastern boundary section is shown in Figures 3a and 3d.

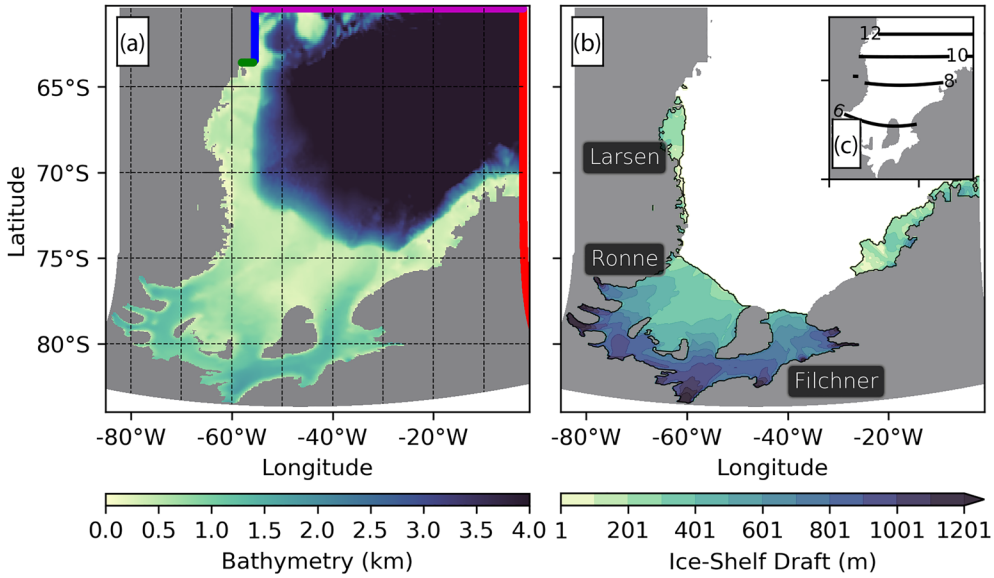

Figure 2. (a) Bathymetry of WED025 with the four ocean boundaries indicated, (b) ice-shelf draft, and (c) grid cell width (km). To reduce computational expense, the Bellinghausen Sea was removed from the simulated domain.

here as a 30-m layer at the top of the cavity (or the entire top level where top levels are thicker than 30 m). All following references to the "top boundary layer" refer to this "Losch" boundary layer (Losch, 2008; Mathiot et al., 2017). Meltwater is treated as a volume flux, that is, it affects the ocean flow divergence near the ice draft. The ice shelf thickness is static, so it is assumed that the ice dynamics instantaneously compensate melt-induced thinning.

The regional NEMO modeling configuration, called "WED025" used in this study (Figure 2) uses a curvilinear grid with a quasi-isotropic horizontal resolution equivalent to approximately 1/4° in longitude; that is, between 3.9 and 13.7 km (grid cell width pictured in Figure 2c). The regional simulation is forced at the surface every 3 h by 10-m winds, 10-m air temperature, 10-m humidity, precipitation, longwave, and shortwave radiation from the 55-year Japanese Reanalysis for driving oceans "JRA55-do" (Tsujino et al., 2018) between 1976 and 2017 through the CORE bulk formulae (Large & Yeager, 2004). For the purposes of this study, we use a new global simulation "G07-JRA" which is forced by JRA55-do, it is otherwise the 1/4° NEMO "G07" configuration, developed by Storkey et al. (2018) with prescribed ice-shelf melting. At the open ocean boundaries, the simulation is forced by temperature, salinity, u/v-velocity, sea surface height, sea-ice thickness/concentration, and snow thickness with monthly means from G07-JRA. For the boundary condition schemes, the Flow Relaxation Scheme algorithm is used for temperature, salinity, velocities and ice fields, and the Flather radiation condition for the depth-mean transports. The initial conditions for WED025 ocean temperature and salinity are taken from G07-JRA March 1976 with the regional model starting with the ocean at rest and no initial sea ice. Following the G07 configuration, G07-JRA is initialized in January 1, 1976 from version 4 of the Met Office Hadley Center objective analysis data set "EN4" (Good et al., 2013). WED025 also has a barotropic tidal forcing as in Jourdain et al. (2019). The four tidal constituents used here (M2, S2, K1, and O1) are lateral ocean boundary conditions interpolated from the global Finite Element Solution FES2012 (Carrère et al., 2012; Lyard et al., 2006). There is no sea surface salinity relaxation in the regional domain but, following the G07 configuration (Storkey et al., 2018), G07-JRA has restoring in the global domain. All simulations in this paper have a common spin-up (1976–1985) where the analysis presented is from 1986–2017.

2.2. WED025 Experimental Design

Experiment 1 is the control "CTRL" simulation with JRA surface forcing in the regional domain and G07-JRA boundary conditions, and is used as the baseline reference for the perturbation experiments. All simulations share the same 1976–1985 spin-up. Figures 1a–1f show that among observational products,

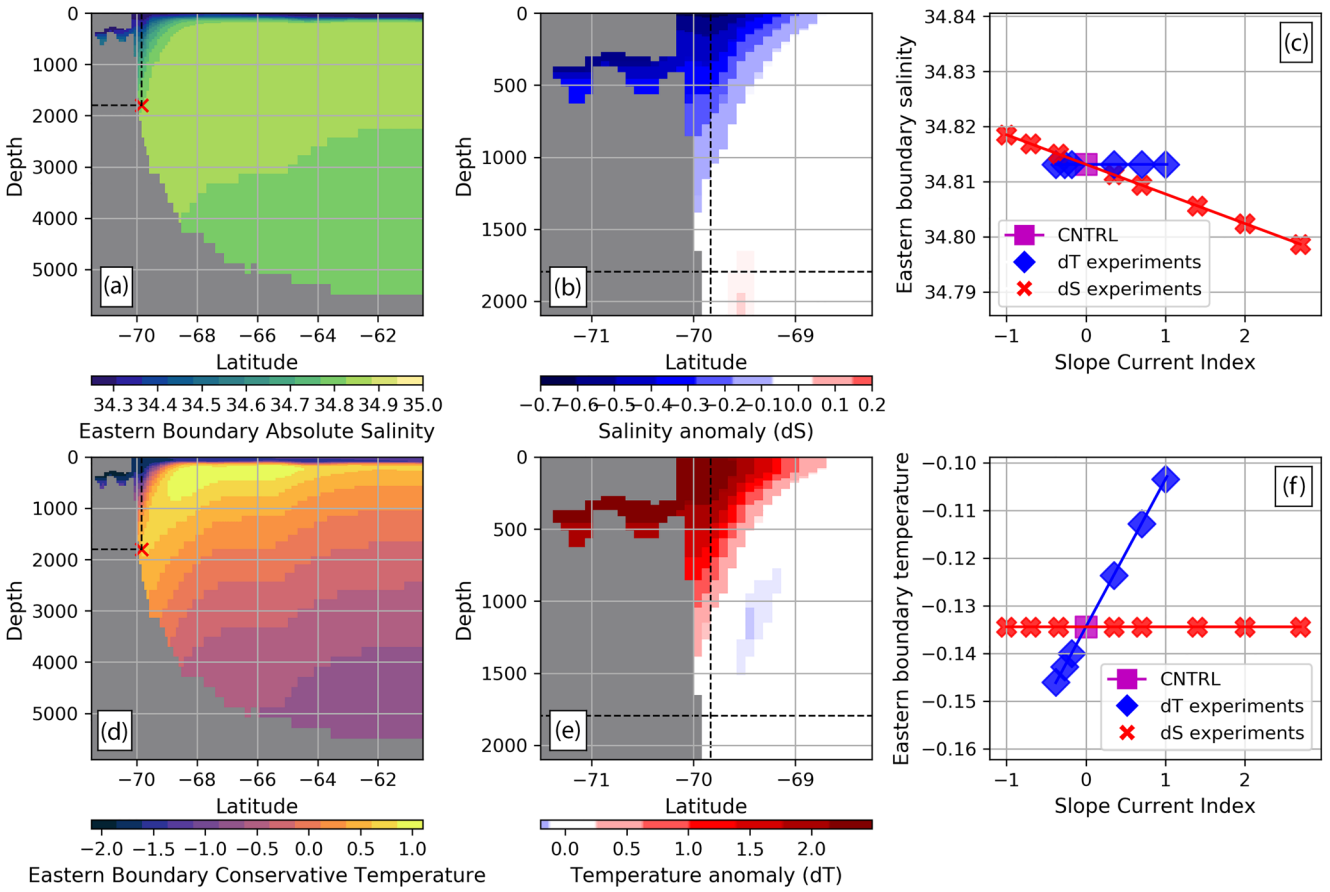

Figure 3. Time-mean WED025 eastern boundary (a) salinity and (d) temperature (eastern boundary is red line Figure 2a). With $M_{\mathrm{CTRL}} = 1$ we have: (b) dS salinity and (e) dT temperature anomalies used to prescribe the water mass perturbations in the ASC across 14 NEMO experiments (Table 1), dashed lines indicate start of Hamming ramps used to smooth perturbation. Simulated eastern boundary (c) salinity and (f) temperature for the 1986–2017 time-mean across all NEMO experiments re-indexed using the Slope Current Index (see Table 1). dS and dT are found by removing ~34.8 and ~0.6 from the CTRL eastern boundary salinity and temperature field (respectively) where these constants are taken from the maximum salinity (red crosses) in the ASC region (dashed) in panel a, see Section 2.2 for further details.

over different time periods, there are considerable differences in the temperature and salinity of the ASC. Additionally, Figure 1g suggests that the ASC is warming and freshening between 1976 and 2017. We will now describe some perturbation experiments that aim to investigate if these kinds of differences influence FRIS ocean circulation and melt rates. As a starting point and to ensure a discernable signal, we consider the 32-year transient response to a step-change perturbation. Our goal is to apply a perturbation that separately modifies the temperature and salinity of the ASC using the CTRL model's time-mean ASC. With this in mind, we create two spatially varying perturbation maps based on the CTRL's ASC temperature and salinity fields: dS and dT for salinity and temperature, respectively. Figures 3b and 3e show dS and dT, which are found by removing ~34.8 g/kg and ~0.555°C from the time-mean eastern boundary salinity, and temperature field, respectively. The salinity and temperature constants used to create dS and dT are the values from the location of maximum salinity within the ASC region (red crosses in Figures 3a and 3d). Additionally, we switch the sign of dT, such that it is shown as a warming pattern and means that dS and dT have a consistent influence on density in the ASC. To isolate the influence of water mass changes in or near the ASC, patterns dS and dT decrease to zero using two Hamming ramps, beginning at 69.8°S and 1795.7 m (dashed lines in Figures 3b and 3e). The ramps were used to minimize unwanted meridional circulation and 69.8°S was chosen to be sufficiently far away from the CTRL's ASC density signature. Additional sensitivity simulations (not shown) suggested that the results were not sensitive to the latitude and depth chosen.

Table 1
List of Experiments.

Number	Name	M_{CTRL}	Slope current index (SCI)
1	CTRL	N/A	0
2	*dS*m1	−1	−1
3	*dS*m07	−0.7	−0.7
4	*dS*m035	−0.35	−0.35
5	*dS*p035	0.35	0.35
6	*dS*p07	0.7	0.7
7	*dS*p14	1.4	1.4
8	*dS*p2	2	2
9	*dS*p27	2.7	2.7
10	dTp1	1	1
11	dTp07	0.7	0.7
12	dTp035	0.35	0.35
13	dTm018	−0.35	−0.18
14	dTm027	−0.7	−0.27
15	dTm038	−1.4	−0.38

Notes. Experiments 13–15 are re-indexed (Figure S1) to account for limiting of the forcing temperature to be above the surface freezing point. The re-index is based on the effective eastern boundary temperature from the time-mean simulation outputs.

Perturbation experiments 2–15 (Table 1) add a temporally constant multiple of dS or dT during 1986–2017 to the time-varying eastern boundary condition. Experiments 2–9 apply a perturbation on the eastern boundary salinity (leaving temperature unchanged) by adding the product of $M_{\mathrm{CTRL}} \times dS$ where M_{CTRL} acts as a multiplier of the CTRL salinity, where M_{CTRL} values are shown in Table 1 and dS in Figure 3b. Similarly, perturbation experiments 10–15 modify the boundary temperature (leaving salinity unchanged) by adding $M_{\mathrm{CTRL}} \times dT$ where M_{CTRL} is again in Table 1 and dT in Figure 3e. In all experiments, U, V and sea surface height are left unchanged; sensitivity experiments (not shown) suggested that these variables only play a minor role on the described results. The dS and dT patterns are negative and positive, so positive M_{CTRL} leads to freshening and warming anomalies, respectively. The range of M_{CTRL} parameter values for adding salt and cooling is limited such that the water column remains stable. In addition, any water mass that would be set below the surface freezing point is instead set to the surface freezing point. Due to this last criterion, when $M_{\mathrm{CTRL}}<0$, the effective temperature perturbation is smaller in magnitude than $M_{\mathrm{CTRL}} \times dT$ so that the boundary temperature never falls below the surface freezing point. To fairly represent all the experiments, the 3 dT experiments with $M_{\mathrm{CTRL}}<0$ are re-indexed to a Slope Current Index (SCI) using the simulated eastern boundary temperature rather than the prescribed $M_{\mathrm{CTRL}} \times dT$, with details shown in Figure S1 (see red values in Table 1 for SCI values). Figures 3c and 3f show that all experiments are linearly related to the SCI in terms of the simulated temperature and salinity on the boundary. All experiments described in this section are listed in Table 1.

3. Results

3.1. Evaluation of the Simulated Weddell Sea Ocean Circulation and FRIS Melt Rates

Figure 4 shows the simulated mean state of the WED025 CTRL simulation. The depth-averaged velocity vectors and barotropic streamfunction (Figures 4a and 4b) show a cavity circulation that is consistent with observations. Specifically, Figures 4a and 4b show an anti-clockwize circulation around Berkner Island (Nicholls et al., 2001) with inflows on the western side of Berkner Island, near the western end of the Ronne Depression and the eastern side of the Filchner Depression (Nicholls et al., 2009; Nicholls & Østerhus, 2004). The narrow outflow along the western edge of the Ronne Depression is also consistent with observations (Nicholls et al., 2004). The spatial pattern of basal refreezing and melting in Figure 4c is similar to satellite-derived estimates (Adusumilli et al., 2020; Joughin & Padman, 2003; Moholdt et al., 2015), where Rignot et al. (2013) are shown in Figure 4i. As a mode 1 ice shelf, the thermal driving (temperature–freezing point) is relatively weak (Figure 4f). In Figure 4c, like the satellite-derived estimates, there is strong melting occurring at the grounding lines and on the southwestern side of Berkner Island, and a large area of refreezing near the center of the Ronne Ice Shelf with smaller areas of refreezing along the western outflows of the Ronne and Filchner cavities. The time-mean (1986–2017) integrated FRIS basal mass loss is 122.3 ± 16.7 Gt/year. This result is within the range of observation-based estimates: 124 ± 66 Gt/year (Moholdt et al., 2015), 83.4 ± 24.8 Gt/year (Joughin & Padman, 2003), and 155.4 Gt/year (113.5 ± 35 Gt/year Ronne and 41.5 ± 10 Gt/year Filchner; Rignot et al., 2013) but higher than the 50 ± 40 Gt/year found by Depoorter et al. (2013). In Figures 4gand 4h, the saltiest, warmest water in the FRIS cavity is found at depth along the western Ronne Depression inflow (east of the smaller outflow), consistent with Gammelsrød et al. (1994). The vertical temperature and salinity structure beneath the ice shelf agrees well with past observations of ocean properties obtained through boreholes (Nicholls et al., 1997, 2001, 1991; Robinson et al., 1994); the modeled temperature (Figures 3d and 3g) and salinity (Figures 3e and 3h) are within 0.1°C and 0.2 g/kg of the observations, respectively.

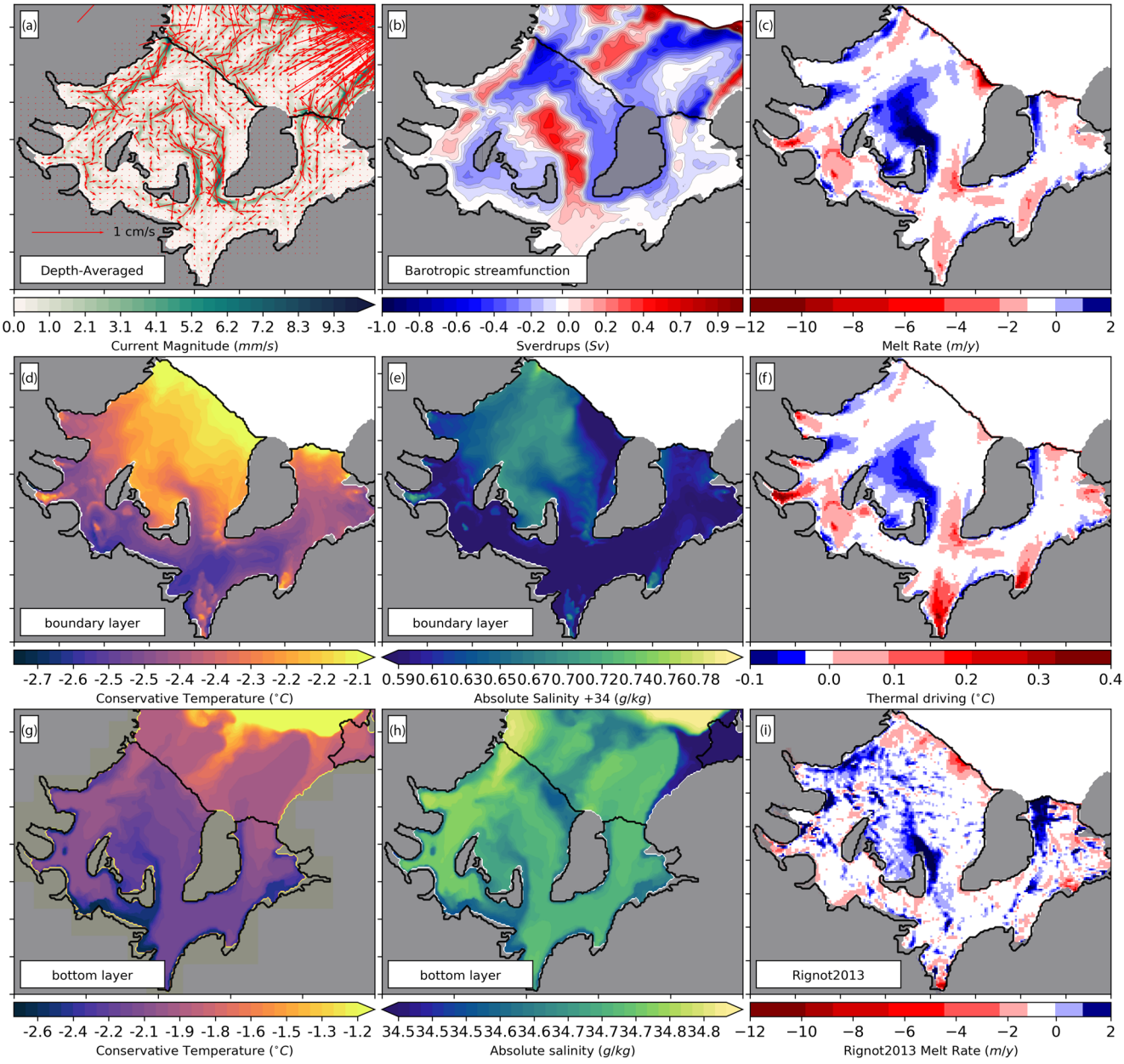

Figure 4. Time-mean conditions for CTRL experiment for: (a) depth-averaged currents, (b) barotropic stream function, (c) melt rate (positive for freezing and negative for melting), (d) ice-shelf boundary layer temperature, (e) ice-shelf boundary layer temperature salinity, (f) thermal driving (temperature in boundary layer—freezing point), (g) deepest ocean cell temperature, (h) deepest ocean cell salinity, (i) Rignot et al. (2013) melt rate.

Satellite-based estimates of ice-shelf basal melting rely on imperfect models and uncertain methods. Satellite estimates combine ice thicknesses and velocity derived from surface elevation data with surface accumulation and firn compaction rates, both of which are either derived from models or are assumed to be constants. Here, we additionally compare the model CTRL simulation to the British Antarctic Survey (BAS) ApRES observations (Nicholls et al., 2015). Details about the collection and processing of the raw data can be found in Vaňková et al. (2020). Whilst ApRES observations are subject to different methodological uncertainty, our estimates are independent of regional climate models and assumptions about firn density. At all sites, the modeled values are consistent with the observations in that they both indicate net melting; melt biases range from 0.09 m yr^{-1} (Site 5c) to 2.3 m yr^{-1} (R08). At nine out of the 14 sites, the melt rate bias is within a factor of two of the observed melt rate. Generally, across all sites, the modeled mean annual melt

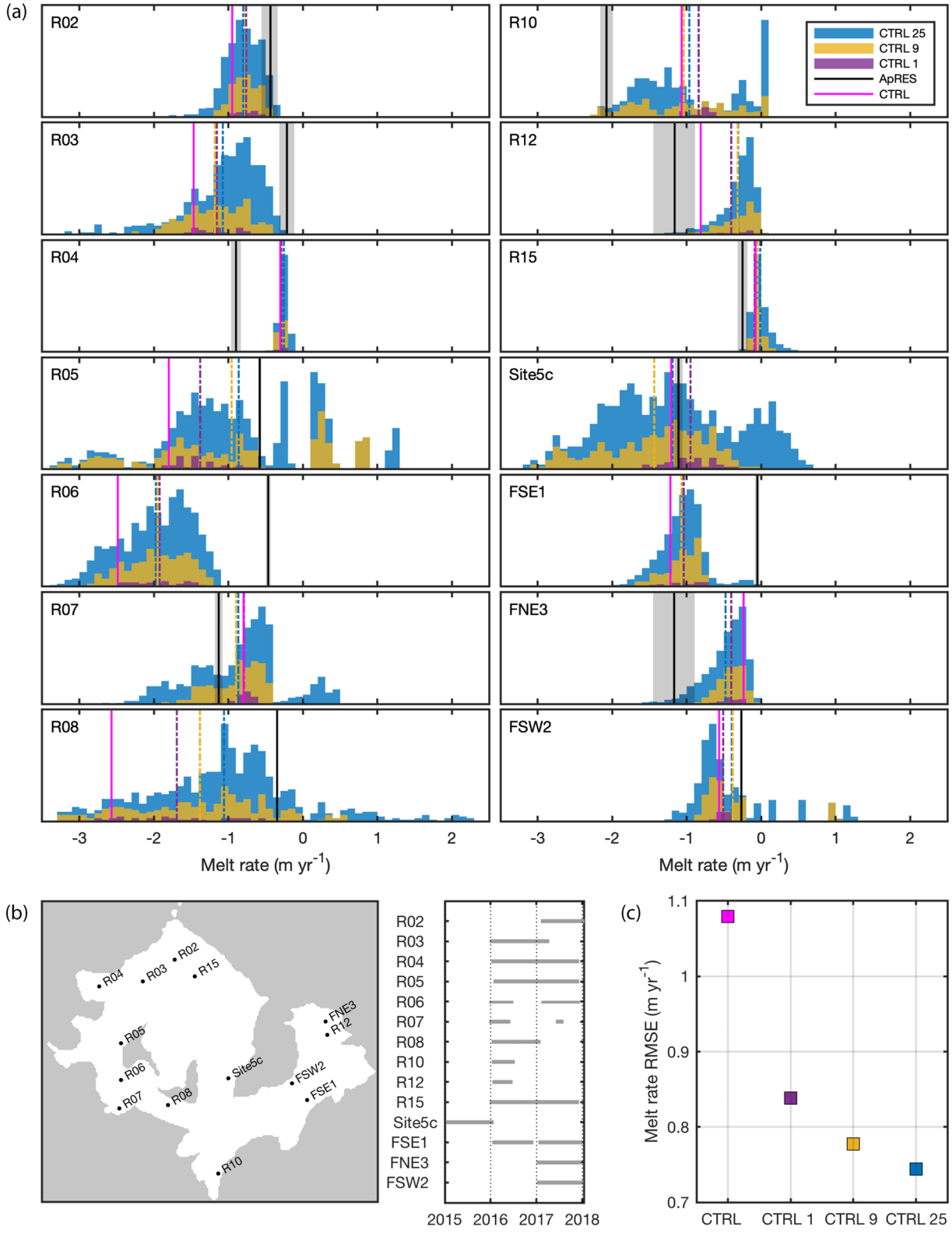

Figure 5. (a) Comparison of Nucleus for European Modeling of Ocean model (NEMO) to autonomous phase-sensitive radio-echo sounder (ApRES) melt rates where the CTRL line (magenta) is the simulated model time-averaged melt rate at the spatial point closest to the ApRES location and matching the time period available. The melt rate is positive for freezing and negative for melting. Histograms show the annual-mean for each available model year with purple, mustard and blue indicating that the closest single (CTRL 1), 9 (CTRL 9), and 25 (CTRL 25) points were used, respectively; the dashed lines are the respective time-mean of all years. (b) location of each ApRES site and time-period available. (c) root mean square error associated with each mean in (a).

rate varies both temporally and spatially, where sites R05, Site5c, and R08 show the largest inter-annual variability. So far, R04, R15, R05, and FSE1 are the only sites with more than one year of data available (2016 and 2017 in Figure 5b), therefore the inter-annual variability of the actual melt rate is largely unknown. Out of these four sites, R05 shows the largest 2016/2017 differences with annual means of −0.50 m yr^{-1} (2016) and −0.67 m yr^{-1} (2017), which is a small difference compared to the year to year variability of the model. Model skill, defined here as the root mean square error (RMSE) between the observed and modeled melt rate, improves the most when taking the time-mean across all modeled years, with an RMSE improvement of 0.24 m yr^{-1} (CTRL–CTRL 1; Figure 5c). Including more adjacent points in addition to all post-spinup modeled years leads to smaller improvements in model skill of between 0.06 and 0.03 m yr^{-1} (CTRL 1–CTRL 9, CTRL 9–CTRL 25, respectively; Figure 5c). In summary, the CTRL simulation, despite its coarse resolution, captures the major (satellite) observed spatial patterns in the time-mean FRIS melt rate where the melt rate magnitude is mostly within a factor of two of the (ApRES) observed melt rate. Whilst some of the CTRL ApRES differences appear to be large, this is an unusually stringent model test and as FRIS is a mode 1 ice shelf with low melt rates, small absolute differences lead to large fractional changes of the mean values.

3.2. Influence of Remote Salinity and Temperature on FRIS Melt Rates

Figures 6a–6c shows the FRIS basal integrated freeze, melt, and net melt rate, respectively, where the time-mean is 1986–2017. Figures 6a and 6b is the main result of this study. First, it shows that melting and freezing in the FRIS is quasi-linearly related to the salinity perturbation (*dS* experiments 2–9 in Table 1) applied to the ASC at the eastern boundary (red line Figure 2a). Second, Figures 6a and 6b shows that changes in temperature (dT experiments 10–15 in Table 1) have a quadratic response in freezing (Figure 6a) and very limited influence on melting (Figure 6b). In other words, a freshening (positive SCI with a *dS* perturbation) of the slope current drives less freezing and melting; whereas a warming (positive SCI with a *dT* perturbation) leads to a decrease in freezing and little change in melting. As net = melt-freeze (Figure 6c) and the *dT* experiments experience little change in melting (Figure 6b), the *dT* experiments show little response under cooling (negative SCI with a *dT* perturbation) but a strong response under warming (positive SCI with a *dT* perturbation). Consistent with Holland et al. (2008), a quadratic polynomial fits all *dT* points in Figure 6c with an r^2 of 1.0. For the *dS* experiments, a freshening leads to less melting/freezing so the net response (Figure 6c) is more symmetric than the *dT* experiments.

The time series (Figures 6d–6g) show that the slope current perturbation (applied over 1986–2017) affects the melting/freezing within the cavity in 1–3 years and returns to the control in cases of smaller perturbations (smaller SCI). With very strong salinity perturbations (e.g., SCI = 2 in Figure 6f) the system does not recover within the simulation timeframe. Dynamical balances will be considered further in Section 3.2. The time series also shows that other processes continue to influence the melting and freezing; for example, in 1998 all experiments show a high melt.

The remainder of this paper will focus on how the *dS* and *dT* experiments modulate melt rate in the cavity. Figures 6a and 6b suggests a quasi-linear relationship between slope current *salinity* and the FRIS time-mean freeze or melt between 1986 and 2017. Similarly, Figures 6a and 6b suggest a quadratic relationship between slope current *temperature* and FRIS freezing with little influence on melting. For net melting in Figure 6c, there is a quasi-linear relationship with changes in slope current salinity and a quadratic with changes in slope current temperature. Figure S2 shows that these relationships are dependent on the time-window chosen. As a starting point, the remainder of this study will focus on finding linear dynamical balances between relevant variables between the 1986-2017 time-mean across the *dS* and *dT* experiments. The more complex transient response is examined in Appendix A and shown in Figures S7–S10.

For readability, all the following comments related to the interpretation of Figures 7–10 will nominally refer to a positive SCI perturbation, namely a freshening or warming for the *dS* or *dT* experiments, respectively. Using a linear regression, Figures 7a and 7d show the spatial map of melt rate change per unit SCI (m/y/SCI) for the *dS* and *dT* experiments, respectively. An ASC freshening (Figure 7a) results in less melting in the melting regions (blue) and less freezing in the freezing regions (red). Comparing Figures 7a–7d, the main difference with a warmer ASC, is that the ice shelf west of Berkner Island melts less rather than more, and the refreezing area in the center of Ronne gets smaller (Figure S3 and S4). This is counterintuitive, as there are increased bottom water temperatures (Figure 9c compared to Figure 8c). Figure 7b shows the

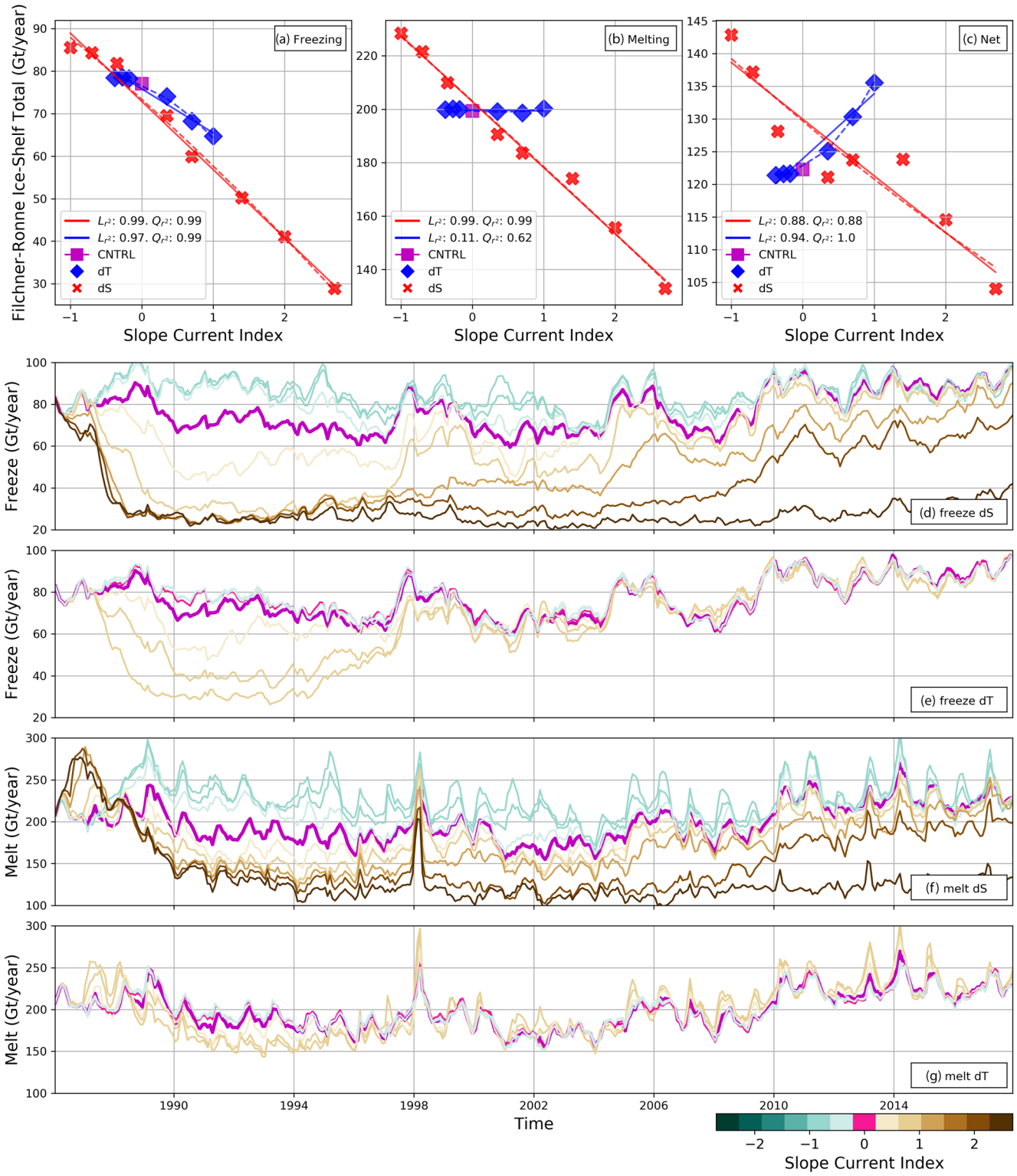

Figure 6. Filchner-Ronne Ice-shelf: (a) freezing, (b) melting, and (c) net, where solid and dashed lines are linear and quadratic regressions. Time-series of freezing: (d) dS and (e) dT experiments, and melting: (f) dS and (g) dT experiments where line color indicates Slope Current Index.

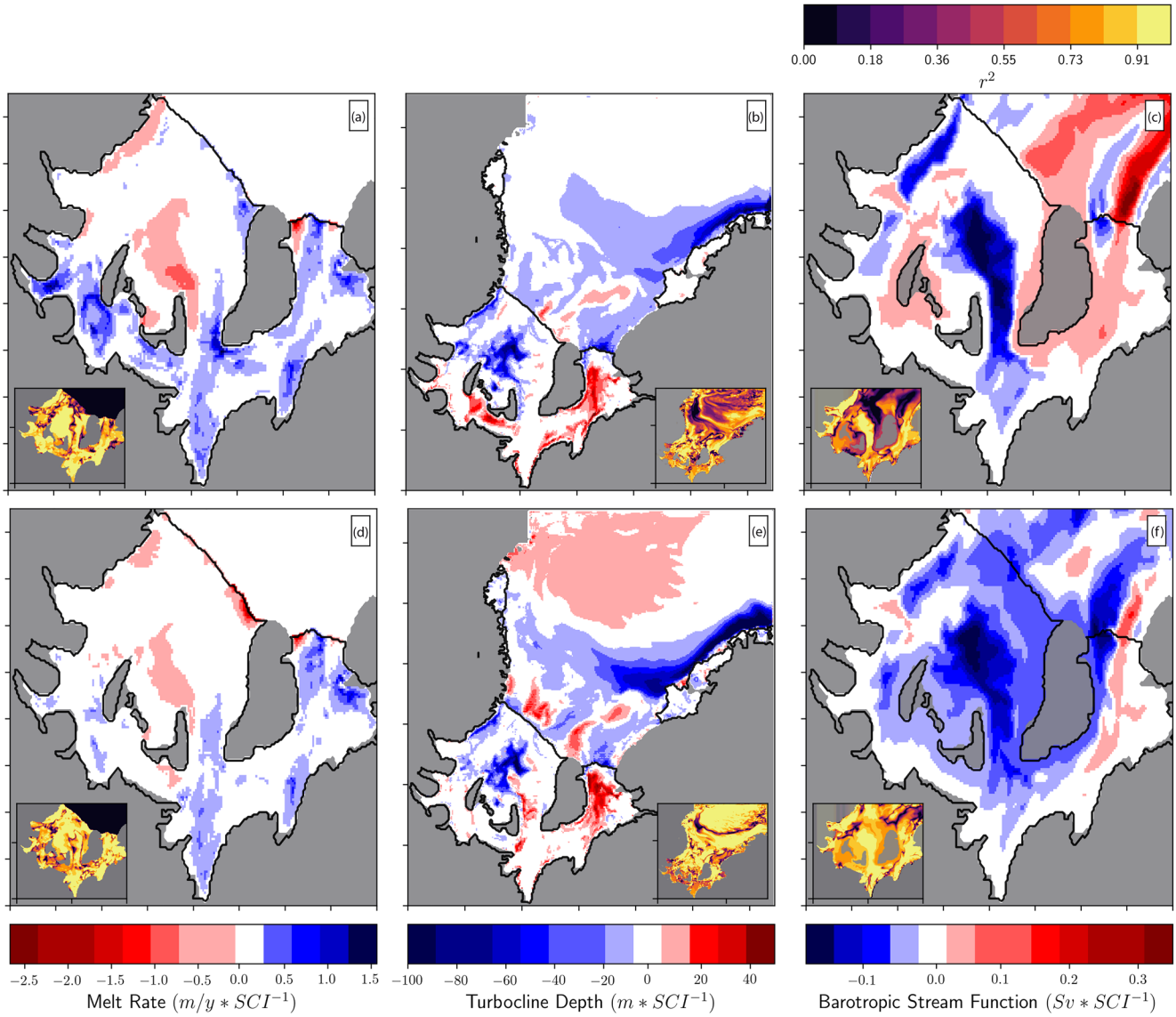

Figure 7. Regression coefficients of three Nucleus for European Modeling of Ocean model (NEMO) variables on SCI between 1986 and 2017 for: (a) ice-shelf freshwater flux, (b) turbocline depth, (c) barotropic stream function, for *dS* experiments. (d–f) as for a-c, but for *dT* experiments. Inset panels show corresponding r^2 value (colorbar top-right). The CTRL ice-shelf freshwater flux is defined negative for melting and positive for freezing (Figure 4c), in (a/d) a positive coefficient in a melting region indicates less melt (a negative coefficient is less freezing in a freezing region) for higher Slope Current Index (SCI). In (b/e) red indicates a lowering and blue a raising of the turbocline for higher SCI.

turbocline depth, which is the depth of the actively mixing layer, defined as the depth at which the vertical eddy diffusivity given by the TKE scheme (see Madec, 2016) falls below a threshold value. A fresher ASC (*dS*; Figure 7b) raises the turbocline along the shelf break and below the freezing regions of the Ronne Ice Shelf. It also lowers the turbocline under the Filchner Ice Shelf. A warmer ASC (dT; Figure 7e) has a similar raised turbocline across the continental shelf break, however, there is a distinct response across the Ronne ice-shelf front with regions of both lowering and raising. In both *dS* and *dT* experiments, a fresher or warmer ASC (respectively) results in a weaker horizontal and overturning circulation in the FRIS cavity (Figures 7c and 7f and Figures 10a and 10b; see Figures 4a and 4b for CTRL horizontal circulation). In the *dS* case, the CTRL circulation is either enhanced or diminished (Figure S5), with a weaker boundary current inflow on the western side of the Ronne (Figures 7c and 10c), a weaker return flow into the freezing region of the Ronne and weaker flow in the southern end of the cavity. In contrast, the *dT* experiments change the horizontal circulation, with a shifted boundary current inflow on the western side of the Ronne (Figures 7f and S6) and a stronger circulation around Berkner Island (Figure S6).

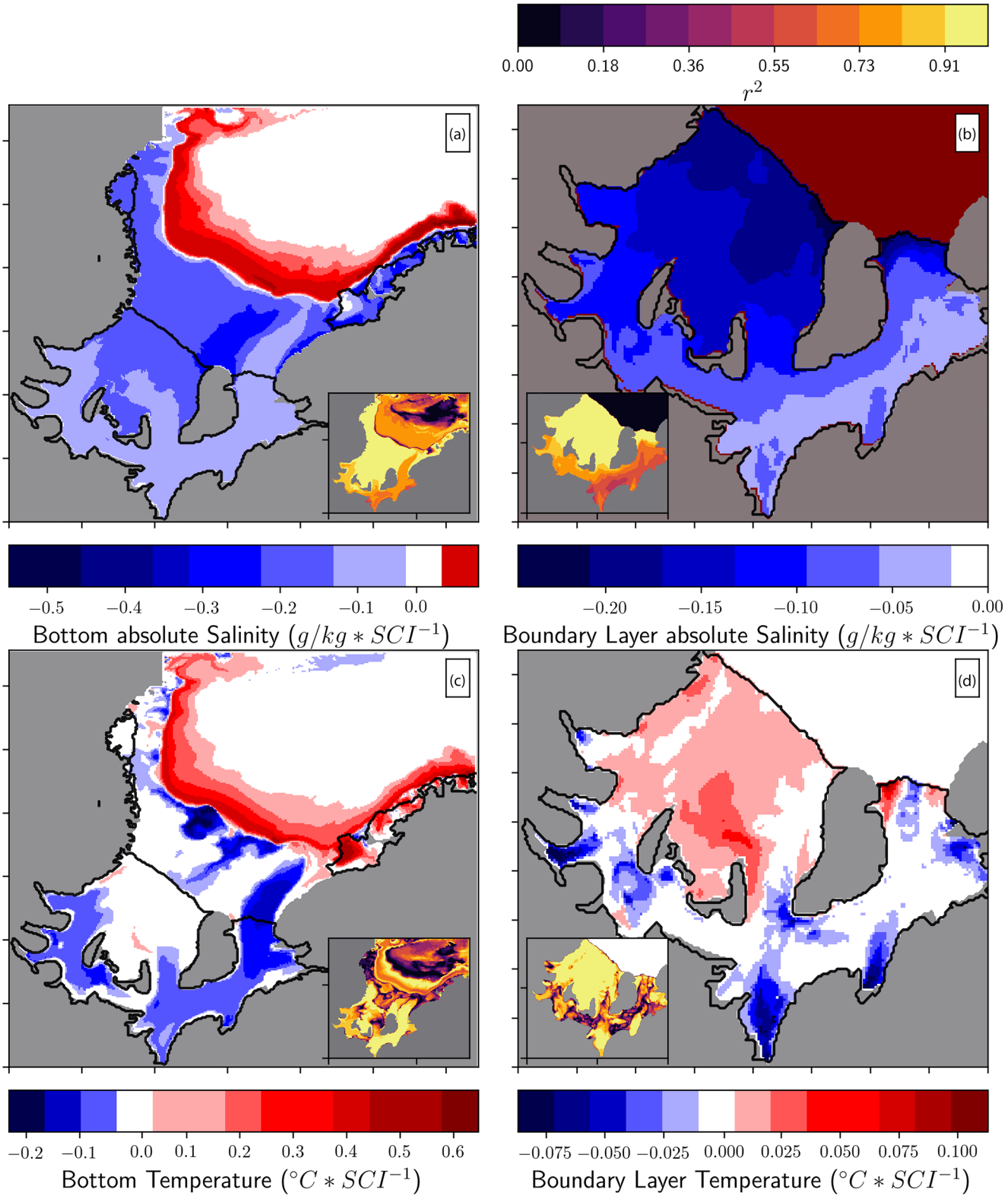

Figure 8. Regression coefficients of four Nucleus for European Modeling of Ocean model (NEMO) variables on Slope Current Index (SCI) as in Figure 7 but now just for *dS* experiments and for: (a) bottom level salinity, (b) top boundary layer salinity, (c) bottom level temperature, and (d) top boundary layer temperature.

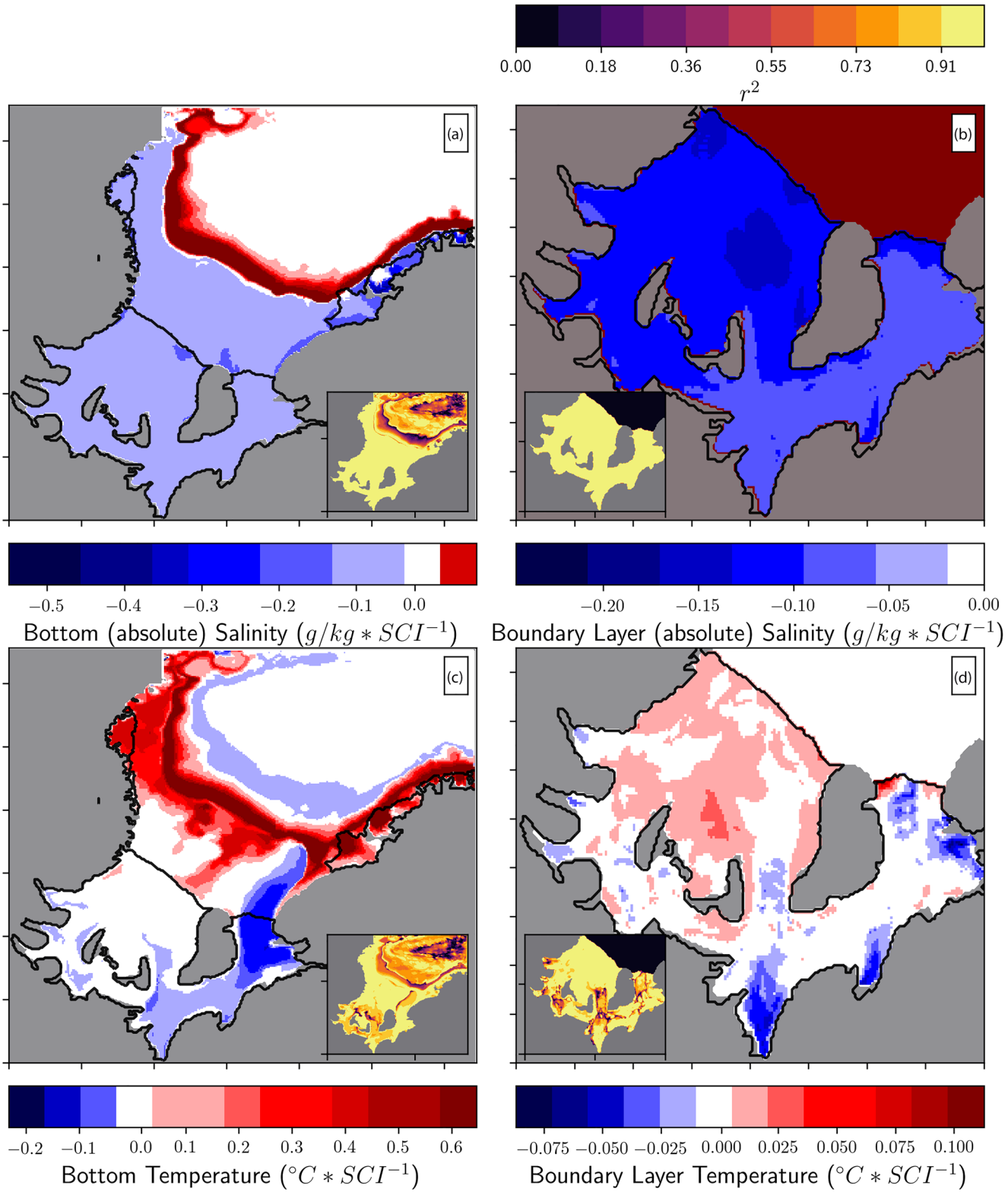

Figure 9. Regression coefficients like in Figure 8 but now for the *dT* experiments.

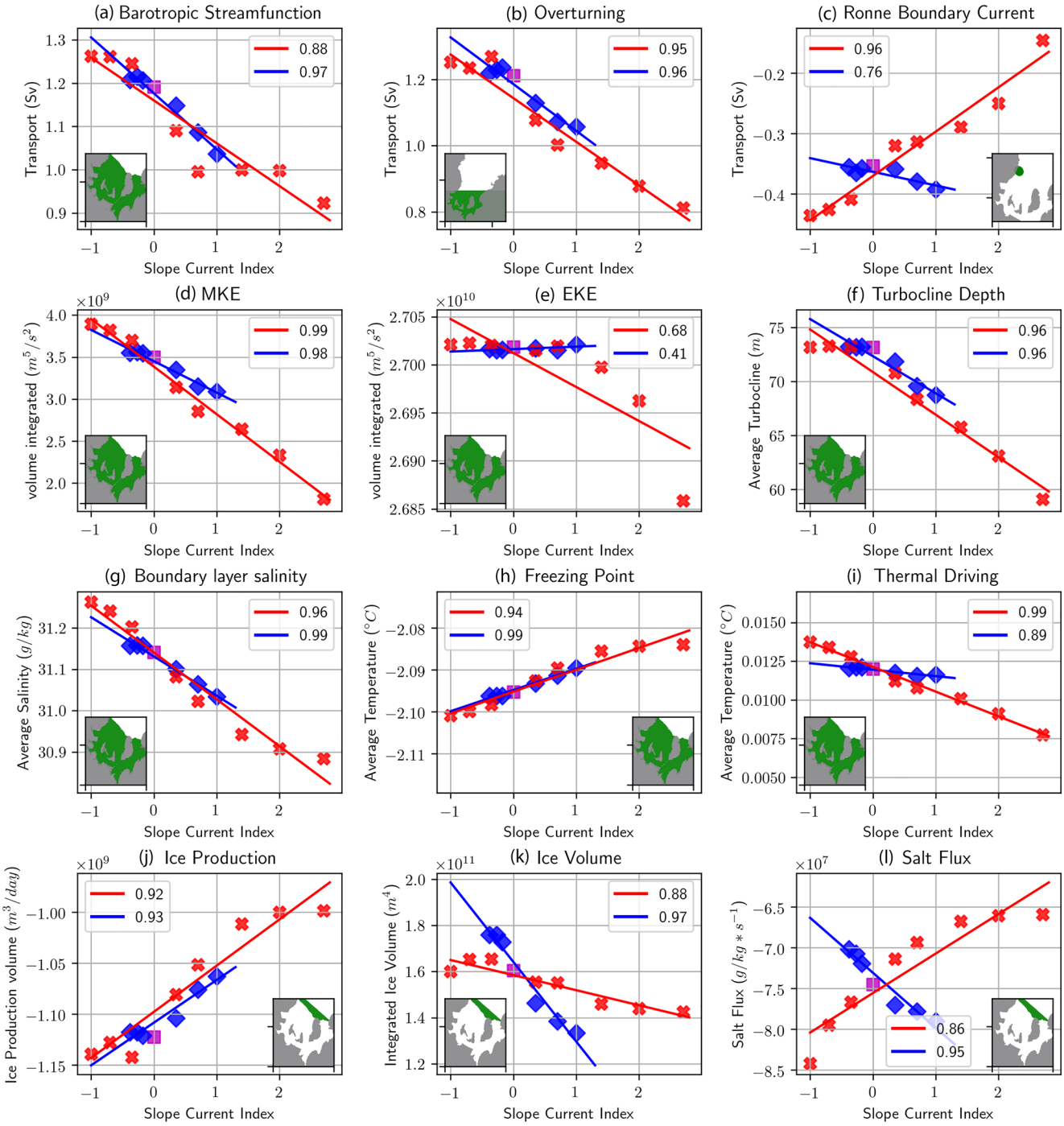

Figure 10. Maximum FRIS amplitude (maximum minus minimum) of: (a) barotropic and (b) meridional overturning streamfunction. (c) Transport across western edge of Ronne ice-shelf front. FRIS volume-integrated boundary layer: (d) Mean Kinetic Energy and (e) Eddy Kinetic Energy. (f) FRIS turbocline depth. (g) Average top boundary layer absolute salinity. (h) Average FRIS freezing point. (i) Average FRIS thermal driving (temperature in top boundary layer—freezing point). Region in front of FRIS front: (j) sea-ice production, and (k) sea-ice volume. Region in which metric is calculated is indicated in inset and metric time window is 1986–2017. dS and dT experiments are red and blue (respectively).

Movies from the dS simulations (Movies S1 and S2) and time series suggest that the freshening signal is advected along the shelf break by the slope current and the near-surface layer freshens in front of Berkner Island and Ronne ice-shelf front (Figure S7). The result is fresher top and bottom water, particularly near the entrance on the Ronne side of the cavity (Figures 8a and 8b). The southwest to northeast freshening

gradient in Figure 8b suggests that the light, fresh layer penetrates as deeply as the ice-shelf geometry allows (bathymetry and ice-shelf draft get deeper toward the back of the cavity, see Figure 2). High r^2 values for the bottom layer and top boundary layer salinity (inset Figures 8a and 8b, respectively) suggest that salinity on the shelf break and Ronne Ice Shelf are largely determined by water mass properties in the slope current (Figures S7g and S7i). The boundary layer temperature changes (Figure 8d) from the *dS* simulations are consistent with less melting and freezing, as we see lower temperatures in melting regions and higher temperatures in freezing regions. Similarly, the cooling of the cavity's bottom water (Figure 8c) is consistent with a weaker cavity circulation, as there is more contact time with the ice-shelf base leading to a net cooling. Many of the spatial patterns are similar in the *dT* experiments under warming (Figure 9); differences from CTRL such as the top boundary layer temperature in Figure 9d and salinity gradients in Figures 9a and 9b are consistent with the described changes in circulation in Figure 8. The main difference between *dS* and *dT* perturbations is in the bottom temperatures (Figures 8c and 9c), where the flow along the continental shelf and across the Ronne depression warms rather than cools. This will be revisited in the discussion (Section 4) and Appendix A.

Figures 10a–10c and 10f provide further evidence of the changes in cavity circulation we have discussed in Figures 7–9, now shown as integrated or averaged quantities. Specifically, a fresher or warmer ASC (*dS* or *dT* experiments, respectively) leads to a quasi-linear weakening in the cavity circulation (barotropic and overturning; Figures 10a and 10b, respectively) with a weaker inflow from the western Ronne Depression boundary current in the *dS* case (Figure 10c) and an overall raising of the turbocline (Figure 10f). Figures 10d and 10e show the top boundary layer volume integrated mean and eddy kinetic energy, defined by $\mathrm{MKE} = \frac{1}{2}\int_V \left(\overline{u}^2 + \overline{v}^2\right) dV$ and $\mathrm{EKE} = \frac{1}{2}\int_V \left(\overline{u'}^2 + \overline{v'}^2\right) dV$ (respectively), where $\overline{u}$ and $\overline{v}$ are the time-mean horizontal velocity components and u' and v' are the time-varying horizontal velocity components. Given the coarse resolution of WED025 compared to the Rossby radius (Hallberg, 2013), we do not expect EKE to be generated by resolved "eddies"; EKE here, encapsulates any velocity fluctuation that deviates from the time-mean. Indeed, via ensemble averaging (e.g. $\overline{u'u'} = \overline{uu} - \overline{u}\,\overline{u}$), EKE includes the influence of tides as the relevant square terms are accumulated online at every model time-step (720 seconds). Since the tides dominate (Hausmann et al., 2020; Makinson et al., 2011; Mueller et al., 2018) the modulus of the velocity field in the FRIS cavity, and the barotropic tides are unchanged across the experiments, it is unsurprising that the EKE is mostly unchanged, with a very small relative reduction in EKE under a strong positive SCI with *dS* (Figure 10e). In contrast, in Figure 10d, MKE shows a large, quasi-linear reduction with an increasingly fresher or warmer ASC. Figures 10g–10i show a quasi-linear change in salinity in the boundary layer with a related raising of the freezing point and reduced thermal driving. Figures 10j and 10k suggest that the weaker circulation in the *dS* and *dT* experiments for positive SCI could be due to the freshening shutting down the supply of dense HSSW on the continental shelf. Theoretically, a reduction in the annual pulse of brine rejection would lead to less HSSW being produced on the continental shelf and less dense water flowing into the ice-shelf cavity. HSSW is relatively warm compared to ISW; by having less HSSW in the cavity, this leads to less melting and a weaker circulation, as suggested by Nicholls (1997). Specifically, Figures 10j and 10k show that a freshening coincides with a reduction in sea-ice production and sea-ice volume on the continental shelf. Drivers of the different responses to *dS* and *dT* perturbations will be discussed in the next section.

4. Discussion

The complex transient response is examined in Appendix A and shown in Figures S7–S10. We found that understanding the transient response is what provided us with key supporting evidence for understanding the time-mean response described here. Brief reference is made to the transient response where appropriate in this discussion.

4.1. Metrics that Could Explain the Simulated Changes in the FRIS Melt Rate

To attribute the relative importance of the phenomena discussed above and in Section 3.2 we show the time-mean percentage change of key metrics from the CTRL simulation in Table 2. Since EKE is almost

Table 2
Percentage Change From CTRL for dS and dT Experiments in Terms of Quantities Shown in Figure 6 (Time-Mean Integrated FRIS Freeze, Melt, and Net Melt Rate) and Figure 10 (Barotropic Streamfunction, Overturning, Mean Kinetic Energy, and Thermal Driving)

Experiment	Freeze	Melt	Net	Barotropic Streamfunction	Overturning	Mean Kinetic Energy	Thermal driving
*dS*m1	11.0	14.6	16.9	6.0	3.4	11.4	14.6
*dS*m07	9.4	11.1	12.2	5.9	2.0	9.3	11.7
*dS*m035	6.2	5.3	4.8	4.5	4.8	5.8	6.6
*dS*p035	−9.8	−4.4	−0.9	−8.5	−11.0	−10.2	−6.4
*dS*p07	−22.3	−7.9	1.2	−16.4	−17.3	−18.3	−10.0
*dS*p14	−34.8	−12.7	1.3	−16.0	−21.7	−24.3	−15.9
*dS*p2	−46.7	−21.9	−6.3	−16.2	−27.5	−33.2	−24.0
*dS*p27	−62.5	−33.3	−14.9	−22.5	−33.0	−48.2	−35.4
dTm038	1.8	0.3	−0.7	1.4	0.7	0.7	0.6
dTm027	2.0	0.4	−0.5	2.0	1.6	1.6	0.9
dTm018	1.6	0.3	−0.5	1.3	2.1	2.1	0.9
dTp035	−3.9	−0.1	2.3	−3.6	−6.8	−6.8	−2.1
dTp07	−11.4	−0.4	6.6	−8.8	−11.5	−11.5	−3.7
dTp1	−16.0	0.5	10.9	−13.0	−12.7	−12.7	−3.0

unchanged across the *dS* and *dT* experiments (see Section 3.2), we focus here on changes in MKE. In the *dS* and *dT* experiments, changes in the mean circulation (barotropic streamfunction, overturning, and MKE) are of a similar magnitude to changes in freezing. Similarly, for the *dT* experiments, the mean circulation (barotropic streamfunction, overturning, and MKE) is of a similar magnitude to the changes in melting. This suggests, that changes in ice-shelf cavity circulation could be relevant in driving the changes in the net melt rate. As FRIS is in a cold-water regime, its mean thermal driving in the CTRL simulation is low at ∼0.01°C. Table 2 shows that the thermal driving changes for the *dS* experiments are large when referenced from the CTRL (+15% for *dS*m1 and −35% for *dS*p27). Interestingly, this is not the case for the *dT* experiments, where the change in thermal driving has a small but opposite sign to the net melt rate changes (0.6% dTm038% and −3% for dTp1). This may be because, in the *dT* experiments, net melt rate differences are largely from changes in freezing rather than from melting (Table 2 and Figure 6, and slowdown of Ronne ice-shelf cavity circulation in Figure S10). In summary, in the *dS* experiments, changes in melt rate are driven by changes in the mean ice-shelf cavity circulation and thermal driving, whereas in the *dT* experiments the melt rate changes are driven by ice-shelf cavity circulation changes.

Recall that the *dT* experiments show a quadratic freezing relationship to changes in ASC temperature with no change in melting in FRIS (Figures 6a–6c). In Figure 10, the *dT* experiments with a warmer ASC show a weaker ice-shelf cavity circulation strength and only small changes in thermal driving; this is consistent with a change in freezing alone (not melting) and can be explained as follows. Heat and salt diffusion across the boundary layer regulate the melt rate. In the freezing case, diffusion occurs from the boundary layer toward the relatively cold and fresh seawater. Unlike melting with relatively warm water which is above the local freezing point, freezing on an ice shelf requires a change in the freezing point, which can be achieved by water rising upwards along the ice-shelf base. Thus, the magnitude of freezing (unlike melting) is directly connected to the strength of the overturning circulation.

4.2. Why Do *dS* and *dT* Experiments Have a Different Response?

Using an idealized modeling configuration without tides, Holland et al. (2008) looked at the equilibrated response from changes in far-field temperature to melt rates in an ice-shelf cavity. They found that the thermal driving and ocean flow speed varied linearly with changes in the far-field temperature; the melt rate then is effectively the product of these two terms and so varies quadratically with far-field temperature. This

explanation relies on being in a high melt region where advection of heat is ignored within the boundary layer. Additionally, Holland et al. (2008) found that variations in salinity were unimportant. The idealized configuration and geometry used in their study is most relevant for a mode 2 (warm water regime) ice shelf; there is no continental shelf break, sea ice, and slope current, so the perturbation is applied relatively close to the ice-shelf front. Here, we note that increases in far-field ASC temperature translate to a small decrease in thermal driving (Table 2 and Figure S9b) but overall a quadratic increase in net melting (Figure 6c). Whilst the quadratic increase with changes in ASC temperature appears to be similar to Holland et al. (2008), we believe the response here, particularly the response from ASC salinity, is more complex due to the inclusion of a continental shelf, tides, realistic geometry, and sea ice.

In a mode 2 ice shelf, the melt rate is the main control on the salinity difference between the inflowing and outflowing waters. So when the temperature is raised, increased melting from direct contact with warmer waters at the ice-shelf base enhances the buoyancy forcing on the ice-shelf cavity circulation. At FRIS, or in a mode-1 context, the strength of the ice-shelf cavity circulation is driven by dense water formation at the ice-shelf front (Macayeal, 1984; Nicholls, 1997) and buoyancy gradients between the continental cavity/ISWs. Indeed, freshening and warming both lead to reduced sea-ice production and sea-ice volume near the ice-shelf front. We have found that perturbations to ASC salinity have a straightforward FRIS response (Appendix A), as the perturbation has a direct influence on the shelf salinity (Figure S7g) and thermal driving in the cavity (Figure S9a). Changes in ASC temperature elicit a more complex response, as they do not directly modify the salinity on the continental shelf. Instead, an ASC warming perturbation decreases the amount of sea ice on the continental shelf (Figure S12), which then freshens the continental shelf (Figure S7h) and weakens the ice-shelf cavity circulation (Figure S10b). Conversely, an ASC cooling perturbation increases sea ice, adding salt to the continental shelf, and strengthens the ice-shelf cavity circulation. In summary, freshening the ASC leads to a weaker ice-shelf circulation which lowers melting, but increasing ASC temperature also leads to lower salinity, so the higher temperature perturbation and weaker circulation act against each other, giving a more complex response.

To exclude the influence of tides (which Holland et al., 2008 excluded), experiments 1–11 and 13–15 (Table 1) were re-run without tides. Unfortunately, experiment 12 without tides crashed and could not be recovered. A comparison of Figure S11 (no tides) and Figure 6 (with tides) shows that changes in remote salinity and temperature modulate the net melt rate in both cases; however, the response is stronger when tides are excluded. Changes in temperature now have an influence on melting, and the melting and freezing is not described by a linear relationship. This is consistent with earlier discussion (Section 4.1) regarding the *dT* experiments and can be explained as follows. The strength of the circulation changes the transfer of heat across the boundary layer. When tides are excluded this transfer is no longer dominated by the tides, which means that changes in the circulation strength now have a bigger impact on the melting. As discussed earlier, the amount of freezing is directly tied to the strength of the circulation and changes in the freezing point, and this relationship is true both with and without tides. The response in both melting and freezing in the *dS* experiments (both with and without tides) is different to the *dT* experiments because the *dS* simulations additionally have relatively large changes in thermal driving.

5. Summary and Further Work

In this study, we introduced the NEMO WED025 Weddell Sea regional ocean ice-shelf ocean model configuration. The WED025 historical "CTRL" simulation's mean state was discussed and its estimates of FRIS basal melt rates were evaluated using BAS ApRES observations. As far as we are aware, this is the first study to evaluate an ocean-model configuration with respect to a network of ApRES observations of an ice shelf. The model simulates a melt rate pattern that is similar to satellite-derived estimates and the melt rate is within a factor of two for nine out of the 14 sites when compared to BAS ApRES observations. Twenty-eight sensitivity experiments were then run to examine the influence of changes in remote water properties via the ASC on melt rates in FRIS. Specifically, the ASC's time-mean temperature or salinity are modified through the eastern ocean boundary condition, where the effective perturbation magnitude is according to a "SCI". We find that remote changes in salinity and temperature modulate the time-mean FRIS melting, freezing and net melt rates.

Taking 32-year time-means, we find a quasi-linear change in net melting in FRIS from an ASC salinity (*dS*) perturbation and a quadratic change in net melting in FRIS from an ASC temperature (dT) perturbation.

On the question of FRIS melt rate sensitivity, we quantify the changes in FRIS melt rates in terms of the effective remote change in eastern boundary salinity and temperature (Figure S13); with a linear regression, we find that the net FRIS melt rate varies by $1551\frac{Gt}{y}\frac{\mathrm{g}}{\mathrm{kg}}$ and $327\frac{Gt}{y}\frac{1}{°\mathrm{C}}$, respectively. In both ASC salinity and temperature perturbation cases, the changes in FRIS net melt rates are attributable to changes in the strength of the mean circulation. Additionally, for the ASC salinity experiments (dS), changes in thermal driving are also a factor. We find a stronger response with additional simulations that do not simulate tides. We also show that the response in terms of changes in melt rate is rapid, and transient, with a recovery timescale of 5–15 years dependent on the size of the perturbation where the perturbation is applied throughout the full duration of the simulation. Simulations with very strong ASC salinity perturbations do not revert to CTRL levels in the simulation period. The mechanism behind the recovery is an interesting avenue for further work.

Previous modeling studies of the FRIS region, such as Hellmer et al. (2012, 2017) and Timmermann and Hellmer (2013), have suggested that future climate scenarios may allow warm off-shore waters to reach the FRIS cavity via the Filchner Trough. Ice shelf basal melt rates are rapidly increased through direct contact of warm waters with the ice-shelf base. However, in our present study, large changes in far-field ASC temperatures do not lead to direct contact of this warmer water with the ice-shelf base. Instead, the ASC temperature perturbation modifies the FRIS melt rate indirectly through changes in sea ice production that then influence circulation within the cavity. This suggests, that other factors besides changes in the salinity and temperature of the ASC may be needed to elicit the melt rate response seen by Hellmer et al. (2012). In addition, our study has shown that perturbations in ASC temperature and salinity lead to a distinct, and complex response, involving sea ice, tides, the ocean cavity circulation and the continental shelf break. In particular, the importance of ASC salinity changes confirms that the idealized modeling from Holland et al. (2008) cannot be directly applied in more realistic settings. Interesting future work then, could develop idealized intermediate complexity models.

Our results suggest that ice-shelf/ocean modelers should carefully consider their choice of boundary conditions when running limited area models of the region. In some idealized cases, it has been past practice to use climatological boundary conditions for regional modeling studies (e.g., Hazel & Stewart, 2020; Naughten et al., 2019) but consistency between the boundary conditions and the local forcing is important for realistic representation of inter-annual variability in re-analysis focused studies (e.g., Hausmann et al., 2020). More generally, Figures 1a–1f show differences in the observed and simulated temperature and salinity structure of the ASC across different products/time periods. Improved dynamical understanding and observations of the ASC's time-mean structure, its trends and variability would increase our capacity to simulate realistic melt rates of FRIS.

Our study, has shown that the remote eastern boundary condition can quasi-linearly modulate the water mass properties in the FRIS cavity, its circulation and subsequent melt rates; however, we emphasize that the influence is small in terms of changes to the time-mean melt rate over several decades (Figure S2). That is, local forcing and related processes (e.g., inter-annual variability of the Ronne Polynya and associated HSSW production) are still likely to play the dominant role. However, these results suggest that ice-shelf/ice-sheet modelers interested in creating projections of sea level rise should consider the melt rate sensitivity to remote changes in salinity as well as temperature. Ideally, resulting changes in ocean circulation would also be considered. Additionally of relevance for sea-level rise projections, Figures S3 and S4 show that the 32-year, time-mean melt rate differences from ASC temperature and salinity perturbations, occur in important regions for buttressing (Reese, Gudmundsson et al., 2018).

The present study raises additional questions to pursue toward a better understanding of climate sensitivity of FRIS. Examples include:

- The transient response is quite large compared to the time-mean response. Does the transient response influence melting in buttressing important regions?
- Are melt water feedbacks important for the recovery of FRIS melt rates?
- How does FRIS respond to a perturbation trend in ASC salinity and temperature (compared to the step-change applied here)?

Recent work by Hazel and Stewart (2019) has looked at trends in recent decades in Antarctica's easterly winds. The strength of the easterlies has increased and the seasonality has also been enhanced with stronger winds during winter and weaker during summer. The influence of these trends on the ASC and its water mass properties has yet to be understood. This kind of research is crucial if we wish to improve both past and future simulations of melt rates of FRIS in the Weddell Sea.

Appendix A: FRIS and Continental Shelf Transient Response to Remote ASC Perturbations

Our study focuses on the 1986–2017 time-mean changes. Here, we briefly discuss the transient response, which provides further context for how the remote ASC perturbations interact with the FRIS cavity. Figures S7–S10 show time series of melt rate related diagnostics on the continental shelf and in the FRIS cavity. In the cavity, we focus on the boundary layer speed, temperature, thermal driving, and salinity, as they influence the melt rate. The monthly-averaged top-boundary Kinetic Energy ($\mathrm{KE} = \frac{1}{2}\sqrt{\overline{u}^2 + \overline{v}^2}$ where $\overline{u}, \overline{v}$ are the time-mean horizontal velocity components; Figure S10) is a useful metric here because the modulus of the full velocity (e.g. $u = \overline{u} + u'$) is used for calculating melt at the ice shelf base. Monthly averages will remove the influence of tides (which will dominate EKE as discussed in Figure 10) but encapsulate circulation changes from the CTRL simulation. Figures S7a–S7f show a complex shelf temperature response in terms of changes from perturbed ASC salinity or temperature. In the *dS* experiments (Figures S7a, S7c, and S7e), a fresher ASC leads initially to warmer water on the open continental shelf and in the Ronne ice-shelf cavity (Figures S7a and S7c), concurrently there is increased boundary layer velocities (Figure S9a) and a brief surge in the melt rate (Figure 6f). The increased open continental shelf temperatures reverse around 1994 (Figure S7a) with cooler waters on the open continental shelf and lower melt rates (Figure 6f). The similarities in the time series of melt, thermal driving and boundary layer kinetic energy (Figures 6f and S9a, S10a, respectively) suggest that changes in circulation strength and thermal driving are responsible for the changes in the *dS* melt rate. In the *dT* experiments, a warmer ASC generally leads to a warmer shelf but, curiously, a cooling of the ASC also leads to a warmer shelf. Like the *dS* experiments (Figure S7e), the Filchner ice-shelf cavity shows the clearest *dT* response (Figure S7f) with a warmer ASC leading to a cooling of the Filchner ice-shelf cavity (see also Figure 9c). The temperature evolution in the top boundary layer in each experiment is consistent with both the *dT* and *dS* changes in melt rate (Figures S8a–S8f). The evolution of salinity on the shelf (Figures S7g–S7h), in the FRIS cavity (Figures S7i–S7l) and boundary layer (Figure S8g-S8l) is straightforward in both the *dS* and *dT* experiments; a freshening or warming leads to fresher waters on the shelf and in the FRIS cavity.

Data Availability Statement

Computational resources were provided by the ARCHER UK National Supercomputing Service and the MONSooN system. The latter is a collaborative facility supplied under the Joint Weather and Climate Research Programme (JWCRP), a strategic partnership between the Met Office and NERC. The WED025 simulation output created for this study is available on the CEDA Archieve: https://doi.org/10.5285/5F9E37B3-AF39-4190-99A8-8AF84EA51D88 (Bull, 2020). The scripts used to prepare the regional model configuration, and model components are available on https://doi.org/10.5281/zenodo.3909234. The WED025 configuration is also the basis of a new NEMO trunk reference configuration: https://zenodo.org/record/3767939. B-SOSE as used here is evolved from Verdy and Mazloff (2017).

Acknowledgments
The authors would like to thank David R. Munday, Antony Siahaan, and Xylar Asay-Davis for helpful discussions while setting up the modelling configuration and running G07-JRA. This research was supported by the UK Natural Environment Research Council (NERC) through the Filchner Ice Shelf System project (NE/L013770/1) and the European Union's Horizon 2020 research and innovation programme under grant agreement no. 820575 (TiPACCs). N. Jourdain is funded by the French National Research Agency (ANR) through the TROIS-AS project (ANR-15-CE01-0005-01). I. Vaňková received funding from the European Union's Horizon 2020 research and innovation programme under the Marie Sklodowska-Curie grant (agreement 790062). J. B. Sallée and U. Hausmann were funded by the European Research Council (ERC) under the European Union's Horizon 2020 research and innovation program (grant agreement 637770). U. Hausmann moreover acknowledges funding by CNES. The authors also acknowledge the JWCRP Joint Marine Modelling Programme for providing support and access to model configurations and output. The authors thank Ronja Reese for advice on the use of buttressing flux response numbers from Reese, Gudmundsson et al. (2018) and Jeremie Mouginot for kindly sharing data from (Rignot et al., 2013). The authors thank Xylar Asay-Davis for his detailed review feedback and interest, which contributed to the quality of this manuscript. The authors also thank an anonymous reviewer for their constructive comments.

References

Adusumilli, S., Fricker, H. A., Medley, B., Padman, L., & Siegfried, M. R. (2020). Interannual variations in meltwater input to the Southern Ocean from Antarctic ice shelves. *Nature Geoscience*, *13*(9), 616–620. https://doi.org/10.1038/s41561-020-0616-z

Asay-Davis, X. S., Cornford, S. L., Durand, G., Galton-Fenzi, B. K., Gladstone, R. M., Hilmar Gudmundsson, G., et al. (2016). Experimental design for three interrelated marine ice sheet and ocean model intercomparison projects: MISMIP v. 3 (MISMIP +), ISOMIP v. 2 (ISOMIP +) and MISOMIP v. 1 (MISOMIP1). *Geoscientific Model Development*, *9*(7), 2471–2497. https://doi.org/10.5194/gmd-9-2471-2016

Asay-Davis, X. S., Jourdain, N. C., & Nakayama, Y. (2017). Developments in simulating and parameterizing interactions between the Southern Ocean and the Antarctic ice sheet. *Current Climate Change Reports*, *3*(4), 316–329. https://doi.org/10.1007/s40641-017-0071-0

Barnier, B., Madec, G., Penduff, T., Molines, J. M., Treguier, A. M., Le Sommer, J., et al. (2006). Impact of partial steps and momentum advection schemes in a global ocean circulation model at eddy-permitting resolution. *Ocean Dynamics*, *56*(5–6), 543–567. https://doi.org/10.1007/s10236-006-0082-1

Bull, C. (2020). *WED025DATA—Weddell Sea limited region ocean ice shelf model (NEMO) data*, Natural Environment Research Council's Data Repository for Atmospheric Science and Earth Observation and UK Polar Data Centre. Retrieved from https://doi.org/10.5285/5F9E37B3-AF39-4190-99A8-8AF84EA51D88

Carrère, L., Lyard, F., Cancet, M., Guillot, A., & Roblou, L. (2012). FES2012: A new global tidal model taking advantage of nearly 20 years of altimetry. *Proceedings of the "20 Years of Progress in Radar Altimetry" Symposium* (pp. 1–20). Venice.

Daae, K., Darelius, E., Østerhus, S., & Ryan, S. (2018). Wind stress mediated variability of the Filchner trough overflow, Weddell sea. *Journal of Geophysical Research: Oceans*, *123*(5), 3186–3203. https://doi.org/10.1002/2017JC013579

Daae, K., Hattermann, T., Darelius, E., & Fer, I. (2017). On the effect of topography and wind on warm water inflow—An idealized study of the southern Weddell Sea continental shelf system. *Journal of Geophysical Research: Oceans*, *122*, 2622–2641. https://doi.org/10.1002/2016JC012541

Darelius, E., & Nicholls, K. W. (2016). Observed vulnerability of Filchner-Ronne Ice Shelf to wind-driven inflow of warm deep water. *Nature Communications*, *7*, 1–7. https://doi.org/10.1038/ncomms12300

DeConto, R. M., & Pollard, D. (2016). Contribution of Antarctica to past and future sea-level rise. *Nature*, *531*(7596), 591–597. https://doi.org/10.1038/nature17145

Depoorter, M. A., Bamber, J. L., Griggs, J. A., Lenaerts, J. T. M., Ligtenberg, S. R. M., Van Den Broeke, M. R., & Moholdt, G. (2013). Calving fluxes and basal melt rates of Antarctic ice shelves. *Nature*, *502*(7469), 89–92. https://doi.org/10.1038/nature12567

Dinniman, M. S., Asay-Davis, X. S., Galton-Fenzi, B. K., Holland, P. R., & Jenkins, A. (2016). Modeling ice shelf/ocean interaction in Antarctica: A review. *Oceanography*, *29*(4), 144–153.

Donat-Magnin, M., Jourdain, N. C., Spence, P., Le Sommer, J., Gallée, H., & Durand, G. (2017). Ice-shelf melt response to changing winds and glacier dynamics in the Amundsen Sea Sector, Antarctica. *Journal of Geophysical Research: Oceans*, *122*(12), 10206–10224. https://doi.org/10.1002/2017JC013059

Favier, L., Jourdain, N. C., Jenkins, A., Merino, N., Durand, G., Gagliardini, O., et al. (2019). Assessment of sub-shelf melting parameterisations using the ocean—Ice-sheet coupled model NEMO (v3. 6)–Elmer/Ice (v8. 3). *Geoscientific Model Development*, *12*, 2255–2283.

Gammelsrød, T., Foldvik, A., Nøst, O. A., Foldvik, Ø., Anderson, L. G., Fogelqvist, E., et al. (1994). Distribution of water masses on the continental shelf in the Southern Weddell Sea. *Geophysical Monograph Series*, *93*, 159–176. https://doi.org/10.1029/gm085p0159

Good, S. A., Martin, M. J., & Rayner, N. A. (2013). Quality controlled ocean temperature and salinity profiles and monthly objective analyses with uncertainty estimates. *Journal of Geophysical Research: Oceans*, *118*(12), 6704–6716. https://doi.org/10.1002/2013JC009067

Hallberg, R. (2013). Using a resolution function to regulate parameterizations of oceanic mesoscale eddy effects. *Ocean Modelling*, *72*, 92–103. https://doi.org/10.1016/j.ocemod.2013.08.007

Hausmann, U., Sallée, J. -B., Jourdain, N. C., Mathiot, P., Rousset, C., Madec, G., et al. (2020). The role of tides in ocean—Ice-shelf interactions in the southwestern Weddell Sea. *Journal of Geophysical Research: Oceans*, *125*(6), e2019JC015847. https://doi.org/10.1029/2019JC015847

Hazel, J. E., & Stewart, A. L. (2019). Are the near-Antarctic easterly winds weakening in response to enhancement of the southern annular mode? *Journal of Climate*, *32*(6), 1895–1918. https://doi.org/10.1175/JCLI-D-18-0402.1

Hazel, J. E., & Stewart, A. L. (2020). Bi-stability of the Filchner-Ronne ice shelf cavity circulation and basal melt. *Journal of Geophysical Research: Oceans*, *125*(4), e2019JC015848. https://doi.org/10.1029/2019JC015848

Hellmer, H. H., Kauker, F., Timmermann, R., Determann, J., & Rae, J. (2012). Twenty-first-century warming of a large Antarctic ice-shelf cavity by a redirected coastal current. *Nature*, *485*(7397), 225–228. https://doi.org/10.1038/nature11064

Hellmer, H. H., Kauker, F., Timmermann, R., & Hattermann, T. (2017). The fate of the Southern Weddell sea continental shelf in a warming climate. *Journal of Climate*, *30*(12), 4337–4350. https://doi.org/10.1175/JCLI-D-16-0420.1

Holland, P. R., Bracegirdle, T. J., Dutrieux, P., Jenkins, A., & Steig, E. J. (2019). West Antarctic ice loss influenced by internal climate variability and anthropogenic forcing. *Nature Geoscience*, *12*(9), 718–724. https://doi.org/10.1038/s41561-019-0420-9

Holland, P. R., Jenkins, A., & Holland, D. M. (2008). The response of ice shelf basal melting to variations in ocean temperature. *Journal of Climate*, *21*, 2558–2572. https://doi.org/10.1175/2007JCLI1909.1

IOC, S. (2010). In Iapso: The international thermodynamic equation of seawater–2010: Calculation and use of thermodynamic properties, Intergovernmental Oceanographic Commission, Manuals and Guides No. 56 (Vol. 56, pp. 1–196). UNESCO, Manuals and Guides.

Jacobs, S. S., Helmer, H. H., Doake, C. S. M., Jenkins, A., & Frolich, R. M. (1992). Melting of ice shelves and the mass balance of Antarctica. *Journal of Glaciology*, *38*(130), 375–387. https://doi.org/10.3189/s0022143000002252

Jenkins, A., Shoosmith, D., Dutrieux, P., Jacobs, S., Kim, T. W., Lee, S. H., et al. (2018). West Antarctic ice sheet retreat in the Amundsen Sea driven by decadal oceanic variability. *Nature Geoscience*, *11*(10), 733–738. https://doi.org/10.1038/s41561-018-0207-4

Joughin, I., & Padman, L. (2003). Melting and freezing beneath Filchner-Ronne ice shelf, Antarctica. *Geophysical Research Letters*, *30*(9), 1477. https://doi.org/10.1029/2003GL016941

Jourdain, N. C., Asay-Davis, X., Hattermann, T., Straneo, F., Seroussi, H., Little, C. M., & Nowicki, S. (2020). A protocol for calculating basal melt rates in the ISMIP6 Antarctic ice sheet projections. *The Cryosphere*, *14*(9), 3111–3134. https://doi.org/10.5194/tc-14-3111-2020

Jourdain, N. C., Molines, J.-M., Le Sommer, J., Mathiot, P., Chanut, J., de Lavergne, C., & Madec, G. (2019). Simulating or prescribing the influence of tides on the Amundsen Sea ice shelves. *Ocean Modelling*, *133*, 44–55. https://doi.org/10.1016/j.ocemod.2018.11.001

Large, W. G., & Yeager, S. G. (2004). Diurnal to decadal global forcing for ocean and sea--ice models: The data sets and flux climatologies (Technical Report). University Corporation for Atmospheric Research. https://doi.org/10.5065/D6KK98Q6

Losch, M. (2008). Modeling ice shelf cavities in a z coordinate ocean general circulation model. *Journal of Geophysical Research*, *113*(8), 1–15. https://doi.org/10.1029/2007JC004368

Lyard, F., Lefevre, F., Letellier, T., & Francis, O. (2006). Modeling the global ocean tides: Modern insights from FES2004. *Ocean Dynamics*, *56*(5–6), 394–415. https://doi.org/10.1007/s10236-006-0086-x

Macayeal, D. R. (1984). Thermohaline circulation below the Ross ice shelf: A consequence of tidally induced vertical mixing and basal melting. *Journal of Geophysical Research*, *89*(C1), 597–606. https://doi.org/10.1029/JC089iC01p00597

Madec, G. (2016). *NEMO Ocean Engine*, (27 edn.). France: Note du Pole de Modélisation, Institut Pierre-Simon Laplace (IPSL). ISSN No: 1288-1619

Makinson, K., Holland, P. R., Jenkins, A., Nicholls, K. W., & Holland, D. M. (2011). Influence of tides on melting and freezing beneath Filchner-Ronne ice shelf, Antarctica. *Geophysical Research Letters*, *38*(6), 4–9. https://doi.org/10.1029/2010GL046462

Markus, T., Kottmeier, C., & Fahrbach, E. (1998). Ice formation in coastal polynyas in the Weddell Sea and their impact on oceanic salinity. *Antarctic Sea Ice: Physical Processes, Interactions and Variability*, *74*, 273–292.
Mathiot, P., Jenkins, A., Harris, C., & Madec, G. (2017). Explicit and parametrized representation of under ice shelf seas in a z* coordinate ocean model. *Geoscientific Model Development Discussions*, *1*(March), 1–43. https://doi.org/10.5194/gmd-2017-37
Moholdt, G., Padman, L., & Fricker, H. A. (2015). Basal mass budget of Ross and Filchner-Ronne ice shelves, Antarctica, derived from Lagrangian analysis of ICESat altimetry. *Journal of Geophysical Research: Earth Surface*, *2*, S91. https://doi.org/10.1002/2014JF003171
Mueller, R. D., Hattermann, T., Howard, S. L., & Padman, L. (2018). Tidal influences on a future evolution of the Filchner—Ronne ice shelf cavity in the Weddell Sea. *Antarctica*, *12*, 453–476.
Nakayama, Y., Menemenlis, D., Zhang, H., Schodlok, M., & Rignot, E. (2018). Origin of Circumpolar Deep Water intruding onto the Amundsen and Bellingshausen Sea continental shelves. *Nature Communications*, *9*(1), 1–9. https://doi.org/10.1038/s41467-018-05813-1
Naughten, K. A., Jenkins, A., Holland, P. R., Mugford, R. I., Nicholls, K. W., & Munday, D. R. (2019). Modeling the influence of the Weddell Polynya on the Filchner—Ronne ice shelf cavity. *Journal of Climate*, *32*(16), 5289–5303. https://doi.org/10.1175/JCLI-D-19-0203.1
Nicholls, K. W. (1997). Predicted reduction in basal melt rates of an Antarctic ice shelf in a warmer climate. *Nature*, *388*(6641), 460–462. https://doi.org/10.1038/41302
Nicholls, K. W., Corr, H. F. J., Stewart, C. L., Lok, L. B., Brennan, P. V., & Vaughan, D. G. (2015). Instruments and methods: A ground-based radar for measuring vertical strain rates and time-varying basal melt rates in ice sheets and shelves. *Journal of Glaciology*, *61*(230), 1079–1087. https://doi.org/10.3189/2015JoG15J073
Nicholls, K. W., Makinson, K., & Johnson, M. R. (1997). New oceanographic data from beneath Ronne Ice Shelf, Antarctica. *Geophysical Research Letters*, *24*(2), 167–170. https://doi.org/10.1029/96GL03922
Nicholls, K. W., Makinson, K., & Øterhus, S. (2004). Circulation and water masses beneath the northern Ronne Ice Shelf, Antarctica. *Journal of Geophysical Research*, *109*(12), 1–11. https://doi.org/10.1029/2004JC002302
Nicholls, K. W., Makinson, K., & Robinson, A. V. (1991). Ocean circulation beneath the Ronne ice shelf. *Nature*, *354*, 56–58.
Nicholls, K. W., & Østerhus, S. (2004). Interannual variability and ventilation timescales in the ocean cavity beneath Filchner-Ronne Ice Shelf, Antarctica. *Journal of Geophysical Research*, *109*(4), 1–9. https://doi.org/10.1029/2003JC002149
Nicholls, K. W., Østerhus, S., Makinson, K., Gammelsrød, T., & Fahrbach, E. (2009). Ice-ocean processes over the continental shelf of the southern Weddell Sea, Antarctica: A review. *Reviews of Geophysics*, *47*(2007), 1–23. https://doi.org/10.1029/2007RG000250.1
Nicholls, K. W., Østerhus, S., Makinson, K., & Johnson, M. R. (2001). Oceanographic conditions south of Berkner Island, beneath Filchner-Ronne Ice Shelf, Antarctica. *Journal of Geophysical Research*, *106*(C6), 11481–11492. https://doi.org/10.1029/2000JC000350
Núñez-Riboni, I., & Fahrbach, E. (2009). Seasonal variability of the Antarctic Coastal Current and its driving mechanisms in the Weddell Sea. *Deep-Sea Research Part I: Oceanographic Research Papers*, *56*(11), 1927–1941. https://doi.org/10.1016/j.dsr.2009.06.005
Pollard, D., & Deconto, R. M. (2012). Description of a hybrid ice sheet-shelf model, and application to Antarctica. *Geoscientific Model Development*, *5*(5), 1273–1295. https://doi.org/10.5194/gmd-5-1273-2012
Reese, R., Albrecht, T., Mengel, M., Asay-Davis, X., & Winkelmann, R. (2018). Antarctic sub-shelf melt rates via PICO. *The Cryosphere*, *12*(6), 1969–1985. https://doi.org/10.5194/tc-12-1969-2018
Reese, R., Gudmundsson, G. H., Levermann, A., & Winkelmann, R. (2018). The far reach of ice-shelf thinning in Antarctica. *Nature Climate Change*, *8*(1), 53–57. https://doi.org/10.1038/s41558-017-0020-x
Rignot, E., Jacobs, S., Mouginot, J., & Scheuchl, B. (2013). Ice Shelf melting around Antarctica. *Science*, *1*(June), 1–15. https://doi.org/10.1126/science.1235798
Robinson, A., Makinson, K., & Nicholls, K. (1994). The oceanic environment beneath the northwest Ronne Ice Shelf, Antarctica. *Annals of Glaciology*, *20*, 383–390. https://doi.org/10.3189/1994aog20-1-386-390
Rousset, C., Vancoppenolle, M., Madec, G., Fichefet, T., Flavoni, S., Barthélemy, A., et al. (2015). The Louvain-La-Neuve sea ice model LIM3.6: Global and regional capabilities. *Geoscientific Model Development*, *8*(10), 2991–3005. https://doi.org/10.5194/gmd-8-2991-2015
Ryan, S., Hattermann, T., Darelius, E., & Schröder, M. (2017). Seasonal cycle of hydrography on the eastern shelf of the Filchner Trough, Weddell Sea, Antarctica. *Journal of Geophysical Research: Oceans*, *122*(8), 6437–6453. https://doi.org/10.1002/2017JC012916
Spence, P., Holmes, R. M., Hogg, A. M. C., Griffies, S. M., Stewart, K. D., & England, M. H. (2017). Localized rapid warming of West Antarctic subsurface waters by remote winds. *Nature Climate Change*, *7*(8), 595–603. https://doi.org/10.1038/NCLIMATE3335
Storkey, D., Blaker, A. T., Mathiot, P., Megann, A., Aksenov, Y., Blockley, E. W., et al. (2018). UK Global ocean GO6 and GO7: A traceable hierarchy of model resolutions. *Geoscientific Model Development Discussions*, *11*(February), 1–43. https://doi.org/10.5194/gmd-2017-263
Thompson, A. F., Stewart, A. L., Spence, P., & Heywood, K. J. (2018). The Antarctic slope current in a changing climate. *Reviews of Geophysics*, *56*, 1–30. https://doi.org/10.1029/2018RG000624
Timmermann, R., & Hellmer, H. H. (2013). Southern Ocean warming and increased ice shelf basal melting in the twenty-first and twenty-second centuries based on coupled ice-ocean finite-element modelling. *Ocean Dynamics*, *63*(9–10), 1011–1026. https://doi.org/10.1007/s10236-013-0642-0
Tsujino, H., Urakawa, S., Nakano, H., Small, R. J., Kim, W. M., Yeager, S. G., et al. (2018). JRA-55 based surface dataset for driving ocean—Sea-ice models (JRA55-do). *Ocean Modelling*, *130*(December 2017), 79–139. https://doi.org/10.1016/j.ocemod.2018.07.002
Vaňková, I., Nicholls, K. W., Corr, H. F. J., Makinson, K., & Brennan, P. V. (2020). Observations of tidal melt and vertical strain at the Filchner-Ronne Ice Shelf, Antarctica. *Journal of Geophysical Research: Earth Surface*, *126*, 1–16. https://doi.org/10.1029/2019JF005280
Verdy, A., & Mazloff, R. M. (2017). A data assimilating model for estimating Southern ocean biogeochemistry. *Journal of Geophysical Research: Oceans*, *122*, 2647–2651. https://doi.org/10.1002/2016JC012650
Vernet, M., Geibert, W., Hoppema, M., Brown, P. J., Haas, C., Hellmer, H. H., et al. (2019). The Weddell Gyre, Southern ocean: Present knowledge and future challenges. *Reviews of Geophysics*, *57*(3), 623–708. https://doi.org/10.1029/2018RG000604
Webb, D. J., Holmes, R. M., Spence, P., & England, M. H. (2019). Barotropic Kelvin wave-induced bottom boundary layer warming along the West Antarctic Peninsula. *Journal of Geophysical Research: Oceans*, *124*(3), 1595–1615. https://doi.org/10.1029/2018JC014227
Wei, W., Blankenship, D. D., Greenbaum, J. S., Gourmelen, N., Dow, C. F., & Richter, T. G. (2020). Getz Ice Shelf melt enhanced by freshwater discharge from beneath the West Antarctic Ice Sheet. *The Cryosphere*, *14* (4), 1399–1408. https://doi.org/10.5194/tc-14-1399-2020